Master's Thesis

Nonlinear Fokker-Planck collision operator in Rosenbluth form for gyrokinetic simulations using discontinuous Galerkin method

Dongkyu Kim

Department of Nuclear Engineering

Ulsan National Institute of Science and Technology

2023

Nonlinear Fokker-Planck collision operator in Rosenbluth form for gyrokinetic simulations using discontinuous Galerkin method

Dongkyu Kim

Department of Nuclear Engineering

Ulsan National Institute of Science and Technology

Nonlinear Fokker-Planck collision operator in Rosenbluth form for gyrokinetic simulations using discontinuous Galerkin method

A thesis submitted to
Ulsan National Institute of Science and Technology
in partial fulfillment of the
requirements for the degree of
Master of Science

Dongkyu Kim

11.22.2022 of submission
Approved by

_____

Advisor
Eisung Yoon

Nonlinear Fokker-Planck collision operator in Rosenbluth form for gyrokinetic simulations using discontinuous Galerkin method

Dongkyu Kim

This certifies that the thesis of Dongkyu Kim is approved.

11.22.2022 of submission

Signature

_____

Advisor: Eisung Yoon

Signature

_____

Prof. Hee Reyoung Kim

Signature

_____

Prof. Min Sup Hur

Abstract

A gyroaveraged nonlinear collision operator is formulated based on the Fokker-Planck operator in the Rosenbluth-MacDonald-Judd (RMJ) potential form and implemented for the gyrokinetic simulations with the discontinuous Galerkin scheme. The divergence structure of the original RMJ form is carefully preserved throughout the formulation to guarantee the density conservation while neglecting the finite Larmor radius effect. The B-spline finite element method is used to calculate the Rosenbluth potentials for the nonlinear collision operator. In addition to the nonlinear collision operator, linear and Dougherty collision models are also implemented to assess the benefits and drawbacks of each model. For the conservation of the parallel momentum and energy, we adopt a simple advection-diffusion model which numerically enforces the conservation of physical quantities. From bump-on-tail relaxation tests, the monotonically increasing entropy in time and conservation properties are demonstrated for the developed collision operator. Also, a few theoretical predictions for the neoclassical physics such as the neoclassical heat flux, poloidal flow and collisional damping of zonal flow are successfully reproduced by numerical simulations.

Contents

List of Figures

List of Tables

I Introduction

Coulomb collisions are one of the fundamental processes in magnetically confined plasmas. Governing the classical and neoclassical physics of the confined plasmas, they also affect the anomalous transports driven by micro-turbulences. As an essential ingredient for the physics of magnetized plasmas, Coulomb collisions are described by Fokker-Planck operators. Basically, the description and formulation of the operators rely on the characteristics of small angle scatterings. The formulation of the Coulomb collisions has been developed in mathematically two different ways: 1) an integro-differential form by Landau [1] and 2) a form with potentials by Rosenbluth, MacDonald, and Judd (RMJ) [2]. As dictated by physics, the operators obey the H-theorem and also the conservations of mass, momentum, and energy.

Due to intractable nonlinearity of their original forms, however, approximated operators have been developed in a few limiting cases of practical interests. One of widely used operators in practice is a linearized collision operator developed under an assumption that probability distribution function f is close to the Maxwellian distribution function f_M such that $f = f_M + \delta f$, where $\delta f / f_M \ll 1$. In deriving the linearized operators, it is important to make the operators analytically and numerically tractable while retaining correct physical properties, i.e., the conservations of mass, momentum, and energy, and the observance of the H-theorem which means the second law of thermodynamics. Starting from the truncation of higher order terms $\sim O(1/\ln\Lambda)$ [3] in the nonlinear Fokker-Planck operator, which corresponds to $\sim 1/18 \approx 5.6\%$ in conventional tokamak plasma, various physical arguments are applied during the derivations. Here, $\ln\Lambda$ denotes a Coulomb logarithm.

A variety of approximated collision operators have been developed along with continuing improvement efforts - BGK operator [4], Lorentz operator, Lenard-Bernstein [5] or Dougherty operator [6], Lenard-Balescu operator [7, 8], Hirshman-Sigmar operator [9], Abel operator [10] and Sugama operators [11, 12]. One way to approximate the nonlinear Fokker-Planck collision operator is linearization, which splits the operator into a test particle collision part and a field particle collision part. The conservation for the linearized collision operator can be proved by self-adjointness property [3]. Due to computational complexity, the field particle part is frequently ignored in practice. To preserve conservation property of the collision operator in the absence of the field particle part, free parameters are often introduced with additional constraints, through which the conservations are enforced. The Hirshman-Sigmar, Abel, and Sugama operators were derived following this approach. Also, we can reduce the linearized collision operator to the Dougherty operator as shown in Appendix A by retaining only the test particle part of the linearized collision operator in the small speed limit $v/v_{T_s} \to 0$ and consequently neglecting cross-diffusion terms. Here v and $v_{T_s} \equiv \sqrt{T_s/m_s}$ are speed and thermal speed for species s, respectively. Due to the approximation, it was pointed out that the friction of the operator for high energy particles increases with velocity [6, 9].

1.1 Backgrounds

1.1.1 Fusion concept

Currently, several countries including Korea, Japan and the European Union are aiming for carbon neutrality by 2050 to cope with climate change [13]. To this end, global energy consumption continues to increase despite the need to reduce fossil fuels. Therefore, an eco-friendly energy source is needed while satisfying this energy demand. It is expected that fusion power generation can play an important role here. Of course, there are already base power source called nuclear power and eco-friendly renewable energy sources such as solar and wind power. Nevertheless, the reasons for achieving fusion power generation are as follows. First, fission has the problem of storing spent nuclear fuel and the risk of meltdown. Next, renewable energy is less sustainable because it is influenced by nature, or weather. On the other hand, in the case of fusion, there is a problem that neutrons generated by fusion reactions activate wall materials, but it can be minimized by selecting appropriate materials. In addition, deuterium, the main material of nuclear fusion, can be extracted from the sea, and tritium can be extracted from lithium, although it does not exist in a natural state. Therefore, fusion has clear advantages over fission and renewable energy.

The fusion method currently being targeted in the first generation nuclear fusion reactor is a Deuterium-Tritium reaction, and the tritium is radioactive, but it is not a problem unlike that of fission because the half-life is short and only a small amount is used [14]. The reaction formula is as follows.

$$ {}_1\mathrm{H}^2 + {}_1\mathrm{H}^3 \longrightarrow {}_2\mathrm{He}^4 + {}_0\mathrm{n}^1 + 17.6\mathrm{MeV} \tag{1} $$

where ${}_1\mathrm{H}^2$ (or D) is the nucleus of deuterium atom called a deuteron, ${}_1\mathrm{H}^3$ (or T) is the nucleus of tritium atom called a triton, ${}_2\mathrm{He}^4$ (or just α) is the nucleus of helium atom and ${}_0\mathrm{n}^1$ (or just n) is the neutron. Here, α has 3.5 MeV and n has 14.1 MeV, respectively. Tritium extraction from lithium for the D-T reaction is possible with the following reaction.

$$ {}_3\mathrm{Li}^6 + \mathrm{n(slow)} \longrightarrow \alpha + \mathrm{T} + 4.8\mathrm{MeV}, \tag{2} $$

$$ {}_3\mathrm{Li}^7 + \mathrm{n(fast)} \longrightarrow \alpha + \mathrm{T} + \mathrm{n} - 2.5\mathrm{MeV}. \tag{3} $$

Naturally, there are 7.4% of ${}_3\mathrm{Li}^6$ and 92.6% of ${}_3\mathrm{Li}^7$, but since ${}_3\mathrm{Li}^6$ reaction is easier, the reaction with ${}_3\mathrm{Li}^6$ is dominant [15]. Neutron multiplication methods are also needed to prepare for neutron losses that may occur for any reason in fusion process. This is possible by reaction with beryllium or lead and more suitable one is beryllium with the reaction equation as [16]

$$ \mathrm{n} + \mathrm{Be} \longrightarrow 2\mathrm{n} + 2\mathrm{He}^4 - 1.8\mathrm{MeV}. \tag{4} $$

Various conditions are required for fusion reactions, typically temperature, confinement time and density [17]. A very high temperature is required to overcome the repulsive force between atomic nuclei. For the DT reaction, a temperature of approximately 10keV or higher is required. Paradoxically, as the temperature rises, the collision rate decreases because of shorter interaction time, and to solve

this problem, many atoms in the plasma state need to be confined for a long time. There are two typical confinement methods: Magnetic and Inertial confinement. Here, the concept of a magentic confinement device tokamak used in International Thermonuclear Experimental Reactor(ITER) and Korea Superconducting Tokamak Advanced Research(KSTAR) will be described.

The principle of magnetic confinement is as follows. Charged particles obey the Lorentz force $\boldsymbol{F} = q(\boldsymbol{E} + \boldsymbol{v} \times \boldsymbol{B})$ where $\boldsymbol{F}$ is the electromagnetic force, q is the charge, $\boldsymbol{E}$ is the electric field, $\boldsymbol{v}$ is the velocity and $\boldsymbol{B}$ is the magnetic field. The idea of magnetic confinement can be found in the second term of the right hand side. Charged particles under a magnetic field are free in a direction parallel to the magnetic field, but are not free in a vertical direction and move in a circle around the magnetic field. The radius of the circle formed at this time is called Larmor radius and is represented by $r_L = \frac{mv_\perp}{|q|B}$ with mass m and velocity perpendicular to $\boldsymbol{B}$, $v_\perp$. Therefore, under a magnetic field, charged particles perform helical motion around a line of force. Here, to prevent the loss of particles in a direction parallel to the field line, it is the torus-shaped tokamak that connects both ends of the field line.

In the case of the tokamak, the TF(Toroidal Field) coil existing outside creates a magnetic field in the toroidal direction. However, a problem caused by the bent magnetic field occurs, which is a curvature drift $\boldsymbol{v}_R = \frac{mv_\parallel^2}{q} \frac{\boldsymbol{R}_c \times \boldsymbol{B}}{R_c^2 B^2}$ where $v_\parallel$ is the velocity parallel to the $\boldsymbol{B}$ and R_c is the radius of the center of curvature. In addition, the toroidal magnetic field($\boldsymbol{B}_T$), which decreases as it becomes farther from the center, has a gradient in the center direction, which generates a ∇B drift $\boldsymbol{v}_{\nabla B} = \pm\frac{1}{2} v_\perp r_L \frac{\boldsymbol{B} \times \nabla B}{B^2}$ with plus sign for ion and minus sign for electron. In this way, both drifts cause charge separation between electrons and ions, and the electric field generated at this time generates $\boldsymbol{E} \times \boldsymbol{B}$ drift $\boldsymbol{v}_{\boldsymbol{E}} = \frac{\boldsymbol{E} \times \boldsymbol{B}}{B^2}$ and pushes the plasma outward. This problem can be resolved by creating a poloidal magnetic field($\boldsymbol{B}_P$). The charges move along the poloidal direction and then the separated charges are mixed again. The method of making a poloidal magnetic field is possible by electromagnetic induction between the tokamak-centered solenoid and plasma, that is, Faraday's law. The plasma has an electric current and this current creates a $\boldsymbol{B}_P$. Here, the problem is that the generation of plasma current through electromagnetic induction, i.e., the generation of $\boldsymbol{B}_P$, is pulsed operation. Steady operation is required to serve as a base power source and this can be achieved by the bootstrap current generated by plasma itself by the pressure gradient of plasma [18, 19]. Despite the presence of $\boldsymbol{B}_P$, there is a problem that plasma tries to go outside due to internal pressure. To resolve this, additional external vertical field coils are used to suppress the internal plasma pressure by the $\boldsymbol{I} \times \boldsymbol{B}_v$ force and it also adjusts the shape of the plasma. Fig. 1 helps to visually understand the explanation so far. Finally, the heating method of the plasma will be described.

First, there is an ohmic heating. It is a heating method using the resistance generated when a current flows through the plasma to create a poloidal magnetic field. However, as the temperature increases, the resistance decreases, so the heating resulting from this is limited to about 1keV. Therefore, additional heating methods such as Neutral Beam Injection(NBI) heating and Radio Frequency(RF) heating are required for a temperature of 10keV or higher. NBI heating is that neutralizes the accelerated ions using voltage differences and shoots them into the tokamak, and the plasma heats up as these neutral particles collide with the internal plasma particles. RF heating is a method using a resonance phenomenon, and the wave emitted from outside using an antenna heats up the plasma at a region equal to the frequency

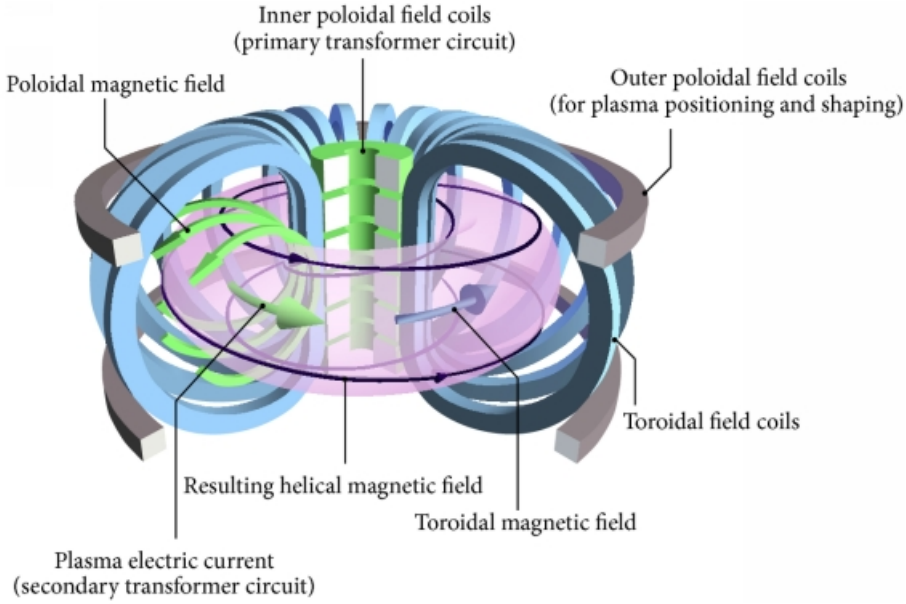

Figure 1: Schematic of a tokamak geometry [20].

of the internal plasma which is $\omega = \frac{qB}{m}$.

1.1.2 Collisional transport

Despite various efforts to confine plasma using magnetic fields, the diffusion of particles and heat takes place in tokamak. There are three main transports: classical, neoclassical and anomalous. It is known that the first two are caused by collisions and the last by turbulence.

First, consider a fully ionized plasma in a straight magnetic field, where the transport of particles and heat can be expressed by the following equations.

$$\boldsymbol{\Gamma} = -D\nabla n \quad : \text{Fick's law} \tag{5}$$

$$\boldsymbol{q} = -\kappa\nabla T \quad : \text{Fourier's law} \tag{6}$$

where $\boldsymbol{\Gamma}$ is the particle flux, D is the diffusion coefficient, ∇n is the density gradient, $\boldsymbol{q}$ is the heat flux, κ is the heat conductivity and ∇T is the temperature gradient. Collisional transports can be described as a random walk argument such as $D \sim \frac{(\Delta x)^2}{\tau}$. Here, Δx is the step length and τ is the time taken the step length. In this case, each coefficient has the following relationship [3]

$$D_\perp \sim \frac{r_L^2}{2\tau}, \quad \kappa_\perp \sim \frac{nr_L^2}{2\tau} \equiv n\chi_\perp \tag{7}$$

where τ is the collision time and $\chi_\perp$ is the heat diffusivity across the magnetic field. We can divide the collision between particles into two cases which are the like-particle collision and the unlike-particle collision. First, like-particle collision do not cause particle transport because collisions between the same species do not change the center of the guiding centers. When a collision occurs between unlike-particles, the particle transport rates of ions and electrons are the same due to the ambipolarity of the

plasma. On the other hand, in the case of heat diffusion, it occurs even in collisions between the like-particles. In this case, the diffusion of heat by the ion-ion collision is the greatest, due to the difference in mass between ions and electrons. Classically, $D_\perp$ is inversely proportional to the square of the magnetic field, but according to actual experimental results, $D_\perp$ is inversely proportional to the magnetic field. This is called Bohm diffusion and is expressed as $D_\perp = \frac{1}{16}\frac{KT_e}{eB} \equiv D_B$ where K is the Boltzmann constant. There are three main causes of this: the possibility of magnetic field errors, the possibility of asymmetric electric fields and the possibility of oscillating electric fields arising from unstable plasma waves [21].

Now let's think about tokamak, which is our interest, the structure where the magnetic field is bent. Inevitably, the inner magnetic field becomes stronger than the outer one, which blocks the movement of particles like a magnetic mirror device. The particles fail to circle in the poloidal direction and draw a new orbit, which is called the banana orbit. Its characteristic length is called the banana width, $\delta r_b \sim \rho_p\sqrt{\varepsilon}$ where $\rho_p = \frac{mv_\perp}{qB_p}$ and $\varepsilon = r/R$ is the inverse aspect ratio with r is the minor radius and R is the major radius. B_p is usually ten times smaller than B, so $D_\perp$ is increased than classical one by our random walk argument and so is $\chi_\perp$, and this is the neoclassical transport.

1.1.3 Discontinuous Galerkin method

The discontinuous Galerkin(DG) method is one of numerical methods to solve differential equations and it can be thought as the combination of finite element method(FEM) and finite volume method(FVM). DG method has some advantages compared to well known numerical methods such as finite difference method(FDM), FVM and FEM. DG method is suitable for complex geometry unlike FDM, it has high-order accuracy and hp-adaptivity contrary to FVM and explicit semi-discrete form in contrast to FEM. Also, of course, it satisfies conservation laws and can be used for elliptic problems like other methods [22] and can easily handle irregular meshes [23]. As the name suggests, the difference from continuous Galerkin method is that DG can have discontinuous basis functions for each element. A simple example follows for reader's understanding from [22, 24].

Consider a 1D wave equation

$$\frac{\partial u}{\partial t} + \frac{\partial f(u)}{\partial x} = 0 \quad \text{on} \quad \Omega \tag{8}$$

where $f(u) = cu$, $\Omega \simeq \Omega_h = \bigcup_{k=1}^{N} D^k$ is the domain and $D^k = \left[x^{k-\frac{1}{2}}, x^{k+\frac{1}{2}}\right]$ is the kth element. Also, we can approximate the solution u as follows

$$u(x,t) \simeq u_h(x,t) = \bigoplus_{k=1}^{N} u_h^k(x,t) \tag{9}$$

$$x \in D^k \quad u_h^k(x,t) = \sum_{i=1}^{N_p} u_h^k(x_i^k,t) l_i^k(x) \tag{10}$$

where $\bigoplus$ means the direct sum, N_p is the local grid points and $l_i^k(x)$ is the Lagrange interpolating polynomial. Multiplying a test function $w(x)$ to the Eq. (8) and integrating it over an element, we can

get the following equation.

$$\int_{D^k} \left(w\frac{\partial u}{\partial t} + w\frac{\partial f(u)}{\partial x} \right) dx = 0. \tag{11}$$

Integrating the above equation by parts and substituting the approximate solution, it becomes

$$\int_{D^k} w_h \frac{\partial u_h^k}{\partial t} dx = \int_{D^k} \frac{\partial w_h}{\partial x} f(u_h^k) dx - \hat{f}\left(u_h^k\left(x^{k+\frac{1}{2}},t\right)\right) w_h\left(x_-^{k+\frac{1}{2}}\right) + \hat{f}\left(u_h^k\left(x^{k-\frac{1}{2}},t\right)\right) w_h\left(x_+^{k-\frac{1}{2}}\right). \tag{12}$$

Here, - and + mean left and right limits, respectively. Since DG allows discontinuity between elements, it is necessary to uniquely determine the flux at the boundary. The numerical flux, $\hat{f}$, is defined as $\hat{f}\left(u_h^k\left(x^{k+\frac{1}{2}},t\right)\right) = \hat{f}\left(u_h^k\left(x_-^{k+\frac{1}{2}},t\right), u_h^k\left(x_+^{k+\frac{1}{2}},t\right)\right)$. Usually, the upwind flux is chosen. In the case of linear flux, the upwind flux is

$$\hat{f}(a,b) = \begin{cases} ca, & \text{if } c \geq 0 \\ cb, & \text{if } c < 0. \end{cases} \tag{13}$$

From this, we can construct matrix equation and obtain the solution. To do that, we set $w_h = l_j^k$ and use Eq. (10) to Eq. (12). Then Eq. (12) becomes

$$\begin{aligned} \int_{D^k} l_i^k l_j^k \frac{\partial u_h^k(x_i^k,t)}{\partial t} dx = \int_{D^k} c u_h^k(x_i^k,t) l_i^k \frac{\partial l_j^k}{\partial x} dx - \hat{f}\left(u_h^k\left(x^{k+\frac{1}{2}},t\right)\right) l_j^k\left(x_-^{k+\frac{1}{2}}\right) \\ + \hat{f}\left(u_h^k\left(x^{k-\frac{1}{2}},t\right)\right) l_j^k\left(x_+^{k-\frac{1}{2}}\right) \quad \text{where} \quad i,j = 1,2,\cdots,N_p. \end{aligned} \tag{14}$$

1.2 Motivation and objective

For a whole device modeling (WDM) of tokamaks, however, it is very important to implement the nonlinear collision operator because the probability distributions in the edge and scrape-off region deviate far from Maxwellian, i.e., the key assumption used in the derivation of the linearized collision operators is no longer valid. There have been dedicated numerical works to solve multi-dimensional nonlinear Fokker-Planck equation for fusion plasma in the Landau form and the RMJ form. The RMJ form was employed by Chacón et al. [25, 26] and Taitano et al. [27] using finite volume methods and by Pataki et al. using a spectral method [28]. The numerical works discretizing the Landau form include a finite volume method used by Yoon et al. [29] and Hager et al. [30] and a finite element method by Hirvijoki et al. [31]. Also, recent works by Francisquez et al. [32] and Hakim et al. [33] employ the Dougherty operator using a discontinuous Galerkin (DG) method. At the time of peer review processes, we have noticed that T. Shiroto et al. [34] published an article about RMJ form of the nonlinear Fokker-Planck operator using a DG method for evolution of an isotropic probability distribution function and Rosenbluth potentials. Since an exhaustive review on all past works related to collision implementation is not in the scope of this thesis, there are other important researches we couldn't mention here for the non-isotropic probability distribution function.

In applying DG methods, there have been growing interests for gyrokinetic whole device modeling of tokamak [33, 35]. DG methods provide many advantages in the gyrokinetic WDM of tokamak plasma. Just listing a few, the methods allow a flexible choice of basis functions to represent numerical solutions, which can exhibit vastly different behaviors depending on simulation region. Especially, in the edge or the scrape-off-layer (SOL) regions of the tokamak, the gradients of density or temperature can be extremely stiff to be treated with the typical grid resolution. The usefulness of the DG method in those stiff gradient regions is demonstrated in the previous gyrokinetic SOL simulations [33, 36]. Also allowing discontinuities of numerical solutions, the methods enable highly localized computing, which can be exploited for an efficient parallelization of simulation. For instance, the core-to-core communication required for the equation of motions based on DG methods is limited to the local exchange of data between neighboring grid cells, instead of the global communication which can be numerically expensive. However, as DG methods are based on the weak form of gyrokinetic equation, terms with derivatives higher than first order are not straightforward to deal with in standard DG methods. Careful and consistent numerical treatments are required for the derivatives still present in the weak form. As nonlinear Coulomb collisions are an essential ingredient in a comprehensive WDM of tokamak plasma, it is highly desired to develop a formulation and numerical scheme for the nonlinear collisions using a DG method.

1.3 Thesis outline

In this work, a nonlinear collision operator based on the Fokker-Planck RMJ form is formulated in gyrokinetic variables and numerically implemented in the DG-based gyrokinetic code [35]. In addition to the nonlinear collision operator, linear and Dougherty collision models are implemented as well to assess the benefits and drawbacks of each model. Also, to analyze characteristics of each collision model in tokamak geometry, a few neoclassical benchmark tests are performed.

The remainder of this thesis is organized as follows. In section II, we present the construction of the gyro-averaged RMJ collision operator and its discretization using the DG method. Section III investigates its numerical properties by comparing the newly implemented operator with the others based on previously known formulations. Section IV shows results of neoclassical verification tests for the newly developed DG collision module in a tokamak geometry. Lastly, conclusions and discussions are given in the last section.

II Numerical method

2.1 The gyroaveraged RMJ collision operator

In the gyrokinetic formalism, the gyroangle is systematically eliminated with gyrokinetic coordinate transformations. By removing the gyroangle, the total number of phase space dimensions is effectively reduced from 6D to 5D. But, it is not trivial to construct collision operators with the finite Larmor radius (FLR) effect and implement such operators numerically. While there are several researches about collision models with FLR effects [11, 37], a simpler model without the FLR effect is used in this work. If we neglect the derivatives with respect to the gyroangle in the RMJ form of Fokker-Planck equation, Eq. (A.1), the gyroaveraged RMJ operator for the self-collision of the ion species a is given as [28]

$$\begin{aligned} C(f_a) = \Gamma_{aa}\frac{\partial}{\partial v_{\parallel o}}\left[-\frac{\partial h_a}{\partial v_{\parallel o}}f_a + \frac{\partial^2 g_a}{\partial v_{\parallel o}^2}\frac{\partial f_a}{\partial v_{\parallel o}} + \frac{\partial^2 g_a}{\partial v_{\parallel o}\partial v_{\perp o}}\frac{\partial f_a}{\partial v_{\perp o}}\right] \\ + \Gamma_{aa}\frac{1}{v_{\perp o}}\frac{\partial}{\partial v_{\perp o}}\left[-\frac{\partial h_a}{\partial v_{\perp o}}v_{\perp o}f_a + \frac{\partial^2 g_a}{\partial v_{\perp o}^2}v_{\perp o}\frac{\partial f_a}{\partial v_{\perp o}} + \frac{\partial^2 g_a}{\partial v_{\parallel o}\partial v_{\perp o}}v_{\perp o}\frac{\partial f_a}{\partial v_{\parallel o}}\right], \end{aligned} \tag{15}$$

$$f_a = -\frac{1}{v_{\perp o}}\frac{\partial}{\partial v_{\perp o}}\left[v_{\perp o}\frac{\partial h_a}{\partial v_{\perp o}}\right] - \frac{\partial^2 h_a}{\partial v_{\parallel o}^2}, \tag{16}$$

$$h_a = \frac{1}{v_{\perp o}}\frac{\partial}{\partial v_{\perp o}}\left[v_{\perp o}\frac{\partial g_a}{\partial v_{\perp o}}\right] + \frac{\partial^2 g_a}{\partial v_{\parallel o}^2}, \tag{17}$$

where $\Gamma_{aa} \equiv 16\pi^2\left(\frac{q_a^2}{m_a}\right)^2 \ln\Lambda_{aa}$ with the Coulomb logarithm $\ln\Lambda_{aa}$. Here, $v_{\parallel o}$, $v_{\perp o}$, q_a and m_a are the parallel velocity, the perpendicular velocity to the background magnetic field, the electric charge and the mass of the species a, respectively. Also, h_a and g_a are the Rosenbluth potentials of the species a. Since we only deal with the self-collision in this work, the species index a will be omitted in the rest of this thesis.

To be implemented in the gyrokinetic simulations, Eq. (15) needs to be transformed from the original coordinate $(\vec{x}, \vec{v}_o)$ to a set of gyrokinetic variables $\vec{z} = (\vec{X}, v_\parallel, u)$ [38]. Here, $\vec{x}$ and $\vec{v}_o$ are the position and the velocity vectors of particles. On the other hand, $\vec{X}$ is a position vector of the gyrocenter and $v_\parallel$ is a parallel velocity of the gyrocenter. Also, u is defined as $\sqrt{2\mu B_0/m}$ where μ and B_0 are the magnetic moment of the gyrocenter and the equilibrium magnetic field at the magnetic axis of tokamak geometry, respectively. Since $du/dt \propto d\mu/dt = 0$ in the Vlasov part of the gyrokinetic equation, u is a natural choice for the velocity coordinate of the gyrokinetic simulation. With this set of variables, the phase space volume $d\vec{x}d\vec{v}_o$ is expressed as $(2\pi/B_0)B_\parallel^* u d\vec{z}$, where $B_\parallel^* \equiv \hat{b}\cdot\left[\mathbf{B} + \frac{mc}{q}v_\parallel \nabla\times\hat{b}\right]$ with the equilibrium magnetic field $\mathbf{B}$ and $d\vec{z} = d\vec{X}dv_\parallel du$. Here, $\hat{b}$ is the unit vector along the equilibrium field and c is the speed of light. $B_\parallel^*$ is the Jacobian of the velocity space, i.e., the density of the phase-space volume element for the gyrokinetic coordinate. In the lowest order of the gyrokinetic ordering, $v_{\parallel o}$ and $v_{\perp o}$ are approximated as $v_\parallel$ and $u\sqrt{B/B_0}$, respectively. From Eq. (15) with this approximation, the

collisional change of $(B_0/2\pi) f d\vec{x} d\vec{v}_o$ can be written as

$$\frac{B_0}{2\pi}\frac{\partial f(\vec{x},\vec{v}_o)}{\partial t} d\vec{x} d\vec{v}_o = C\left(f\left(\vec{X}, v_\parallel, u\right)\right) B_\parallel^* u d\vec{z} \tag{18}$$

$$\approx \Gamma u B_\parallel^* \frac{\partial}{\partial v_\parallel}\left[\left(-\frac{\partial h}{\partial v_\parallel} f + \frac{\partial^2 g}{\partial v_\parallel^2}\frac{\partial f}{\partial v_\parallel} + \frac{B_0}{B}\frac{\partial^2 g}{\partial v_\parallel \partial u}\frac{\partial f}{\partial u}\right)\right] d\vec{z}$$

$$+ \Gamma B_\parallel^* \frac{B_0}{B}\frac{\partial}{\partial u}\left[\left(-\frac{\partial h}{\partial u} u f + \frac{\partial^2 g}{\partial u^2} u \frac{B_0}{B}\frac{\partial f}{\partial u} + \frac{\partial^2 g}{\partial v_\parallel \partial u} u \frac{\partial f}{\partial v_\parallel}\right)\right] d\vec{z} \tag{19}$$

$$= \frac{\partial}{\partial v_\parallel}\left[\Gamma u B_\parallel^*\left(-\frac{\partial h}{\partial v_\parallel} f + \frac{\partial^2 g}{\partial v_\parallel^2}\frac{\partial f}{\partial v_\parallel} + \frac{B_0}{B}\frac{\partial^2 g}{\partial v_\parallel \partial u}\frac{\partial f}{\partial u}\right)\right] d\vec{z}$$

$$+ \frac{\partial}{\partial u}\left[\Gamma B_\parallel^*\left(-\frac{B_0}{B}\frac{\partial h}{\partial u} u f + \frac{B_0}{B}\frac{\partial^2 g}{\partial u^2} u \frac{B_0}{B}\frac{\partial f}{\partial u} + \frac{B_0}{B}\frac{\partial^2 g}{\partial v_\parallel \partial u} u \frac{\partial f}{\partial v_\parallel}\right)\right] d\vec{z}$$

$$- \frac{v_T \partial B_\parallel^*}{B_0 \partial v_\parallel}\frac{1}{v_T}\left[\Gamma u B_0\left(-\frac{\partial h}{\partial v_\parallel} f + \frac{\partial^2 g}{\partial v_\parallel^2}\frac{\partial f}{\partial v_\parallel} + \frac{B_0}{B}\frac{\partial^2 g}{\partial v_\parallel \partial u}\frac{\partial f}{\partial u}\right)\right] d\vec{z}. \tag{20}$$

Note that Eq. (20) is not in a divergence form in the phase space due to the last term which is proportional to $(v_T/B_0)\left(\partial B_\parallel^*/\partial v_\parallel\right)$. In this work, the last term of Eq. (20) is neglected with the assumption of negligible FLR effects, i.e., $(v_T/B_0)\left(\partial B_\parallel^*/\partial v_\parallel\right) \approx (v_T mc)/(B_0 q R_0) \approx \rho/R_0 \ll 1$, where ρ is the gyroradius and R_0 is the major radius of tokamak geometry. With this approximation, Eq. (20) can be written as

$$C\left(f\left(\vec{X}, v_\parallel, u\right)\right) B_\parallel^* u d\vec{z} \approx \frac{\partial}{\partial v_\parallel}\left[u B_\parallel^*\left(-\alpha_1 f + \alpha_2\frac{\partial f}{\partial v_\parallel} + \alpha_5\frac{\partial f}{\partial u}\right)\right] d\vec{z}$$

$$+ \frac{\partial}{\partial u}\left[u B_\parallel^*\left(-\alpha_3 f + \alpha_4\frac{B_0}{B}\frac{\partial f}{\partial u} + \alpha_6\frac{\partial f}{\partial v_\parallel}\right)\right] d\vec{z}, \tag{21}$$

where $\alpha_1 \equiv \Gamma\frac{\partial h}{\partial v_\parallel}$, $\alpha_3 \equiv \Gamma\frac{B_0}{B}\frac{\partial h}{\partial u}$, $\alpha_2 \equiv \Gamma\frac{\partial^2 g}{\partial v_\parallel^2}$, $\alpha_4 \equiv \Gamma\frac{B_0}{B}\frac{\partial^2 g}{\partial u^2}$, $\alpha_5 \equiv \alpha_6 \equiv \Gamma\frac{B_0}{B}\frac{\partial^2 g}{\partial v_\parallel \partial u}$ are introduced for notational simplicity. Although Eq. (21) is an approximated form, two important properties of the original RMJ operator are retained as follows.

1. The divergence form of the original RMJ operator is preserved. This is consistent to the previous work which shows that the linearlized collision operator in the gyrokinetic coordinate can be written in a divergence form when the FLR effect is neglected [39]. The numerical conservation of gyrocenter density can be guaranteed more straightforwardly due to this property.

2. $C(f_M) = 0$ when f_M is the Maxwellian distribution function defined as

$$f_M = \frac{n}{(2\pi)^{3/2} v_T^3}\exp\left[-\frac{\left(v_\parallel - U_\parallel\right)^2 + u^2 B/B_0}{2v_T^2}\right], \tag{22}$$

   where n and $U_\parallel$ are the density and the parallel fluid velocity, respectively.

In addition to the RMJ operator, two simpler models (i.e., the test particle collision and Dougherty model) are also implemented for comparison. The detailed derivation of those models from the RMJ operator is given in A. While the specific expressions for the coefficients α_i are different for each model,

	RMJ model	Test particle collision	Dougherty model
α_1	$\Gamma\frac{\partial h}{\partial v_\parallel}$	$-\bar{\nu}\frac{3\sqrt{\pi}}{8x^3}\left(F_1+3F_2\right)\left(v_\parallel-U_\parallel\right)$	$-\bar{\nu}\left(v_\parallel-U_\parallel\right)$
α_2	$\Gamma\frac{\partial^2 g}{\partial v_\parallel^2}$	$\bar{\nu}\frac{3\sqrt{\pi}v_T^2}{8x^3}\left(F_1+\frac{3\left(v_\parallel-U_\parallel\right)^2}{2v_T^2x^2}F_2\right)$	$\bar{\nu}v_T^2$
α_3	$\Gamma\frac{B_0}{B}\frac{\partial h}{\partial u}$	$-\bar{\nu}\frac{3\sqrt{\pi}}{8x^3}\left(F_1+3F_2\right)u$	$-\bar{\nu}u$
α_4	$\Gamma\frac{B_0}{B}\frac{\partial^2 g}{\partial u^2}$	$\bar{\nu}\frac{3\sqrt{\pi}v_T^2}{8x^3}\left(F_1+\frac{3u^2}{2v_T^2x^2}\frac{B}{B_0}F_2\right)$	$\bar{\nu}v_T^2$
α_5, α_6	$\Gamma\frac{B_0}{B}\frac{\partial^2 g}{\partial v_\parallel\partial u}$	$\bar{\nu}\frac{9\sqrt{\pi}}{16x^5}F_2u\left(v_\parallel-U_\parallel\right)$	0

Table 1: Coefficients α_i of Eq. (21) for each collision model. The detailed derivation for this table is given in A.

all of operators share the same functional form of Eq. (21). Table 1 summarizes the coefficients for each collision model. Here, x, F_1, F_2 and the collision frequency $\bar{\nu}$ are defined as

$$x=\sqrt{\frac{\left(v_\parallel-U_\parallel\right)^2+u^2B/B_0}{2v_T^2}}, \tag{23}$$

$$F_1(x)=x\frac{d\mathrm{erf}(x)}{dx}+(2x^2-1)\mathrm{erf}(x), \tag{24}$$

$$F_2(x)=\left(1-\frac{2}{3}x^2\right)\mathrm{erf}(x)-x\frac{d\mathrm{erf}(x)}{dx}, \tag{25}$$

$$\bar{\nu}=\frac{n\Gamma}{3(2\pi)^{3/2}v_T^3}=\frac{4\sqrt{2\pi}nq^4\ln\Lambda}{3m^2v_T^3}, \tag{26}$$

where $\mathrm{erf}(x)=\frac{2}{\sqrt{\pi}}\int_0^x e^{-t^2}dt$ is the error function.

2.2 The weight evolution equations with DG basis

To be used in DG gyrokinetic simulations, collision operators need to be discretized with the DG basis. While the DG formulation for the Dougherty operator is derived in [32], the generalized version for the RMJ operator is presented in this section. Although Eq. (21) can be discretized on any specific geometry, we only consider the toroidally axisymmetric configuration of tokamak geometry in this work. The cylindrical coordinate $\mathbf{X}=(R,Z,\phi)$ is used, where ϕ is an ignorable variable since the axisymmetry is assumed in the toroidal direction. A poloidal plane in the (R,Z) space is used as the spatial domain which is partitioned with the unstructured triangular mesh. Since the collision operator approximated as Eq. (21) does not induce any flux in the spatial direction of the phase space, the numerical operation for the collision can be performed separately on each spatial cell. Therefore, we formulate the discretization of the collision operator for a single spatial cell Ω_x which has a triangular shape in the (R,Z) space. For the velocity space, the following rectangular domain Ω_v is used.

$$\Omega_v:=\{(v_\parallel,u):v_{\parallel,\min}\le v_\parallel\le v_{\parallel,\max},0\le u\le u_{\max}\}. \tag{27}$$

This velocity domain Ω_v is divided with $N_{v_\parallel}\times N_u$ rectangular mesh, where $N_{v_\parallel}$ and N_u are numbers of cells in the respective directions. Correspondingly, the total phase space $\Omega=\Omega_x\times\Omega_v$ is partitioned with

$\Omega^{[j,k]}$ defined as the Cartesian product $\Omega_x \times [v_{\parallel,j'=j-1}, v_{\parallel,j'=j}] \times [u_{k'=k-1}, u_{k'=k}]$. Here, $j \in \{1,\cdots,N_{v_\parallel}\}$ and $k \in \{1,\cdots,N_u\}$ are cell indices for $v_\parallel$ and u directions, respectively. On the other hand, j' and k' are exclusively used as indices of vertices for $v_\parallel$ and u directions. Also, $v_{\parallel,j'}$ and $u_{k'}$ are the velocity values at vertices and defined as

$$v_{\parallel,j'} \equiv v_{\parallel,min} + \frac{v_{\parallel,max} - v_{\parallel,min}}{N_{v_\parallel}} j', \tag{28}$$

$$u_{k'} \equiv \frac{u_{max}}{N_u} k'. \tag{29}$$

The structure of the single mesh cell $\Omega^{[j,k]}$ is shown in Fig. 2.

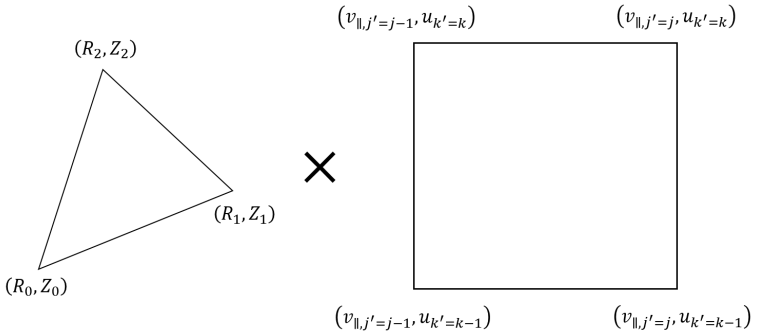

Figure 2: Single mesh cell $\Omega^{[j,k]}$ in the phase space.

In this work, we employ piecewise continuous quadratic polynomials as DG basis functions to represent f in Eq. (21). The corresponding basis function space for $\Omega^{[j,k]}$ is given as

$$V_d = \left\{ \zeta^{[j,k]} : \zeta^{[j,k]}|_{\Omega^{[j,k]}} \in \mathbb{P}_2 \right\}, \tag{30}$$

where $\mathbb{P}_2 = \{R^{l_1} Z^{l_2} v_\parallel^{l_3} u^{l_4} : l_1 + l_2 \leq 2, l_3 + l_4 \leq 2, l_i \in \mathbb{Z}_{\geq 0}\}$ and $\mathbb{Z}_{\geq 0}$ is a set of non-negative integers. With Eq. (30), f can be approximated as

$$f(\vec{z},t) \sim f_d = \sum_{j,k} f_d^{[j,k]}(\vec{z},t), \tag{31}$$

$$f_d^{[j,k]}(\vec{z},t) \equiv \sum_{l'} \hat{f}_{l'}^{[j,k]}(t)\, \zeta_{l'}^{[j,k]}(\vec{z}), \tag{32}$$

where $\vec{z} = (\vec{X}, v_\parallel, u)$. When we multiply Eq. (21) by an arbitrary function $W(\vec{z})$ and take $\int_{\Omega^{[j,k]}} \times$, the following equation is obtained.

$$\begin{aligned}
\int_{\Omega^{[j,k]}} d\vec{z} \left(u B_\parallel^* \right) WC(f) &= \int_{\Omega^{[j,k]}} d\vec{z}\, \mathscr{J} \frac{\partial W f}{\partial t} \\
&= \int_{\Omega^{[j,k]}} d\vec{z} W \frac{\partial}{\partial v_\parallel} \left[\mathscr{J} \left(-\alpha_1 f + \alpha_2 \frac{\partial f}{\partial v_\parallel} + \alpha_5 \frac{\partial f}{\partial u} \right) \right] \\
&+ \int_{\Omega^{[j,k]}} d\vec{z} W \frac{\partial}{\partial u} \left[\mathscr{J} \left(-\alpha_3 f + \alpha_4 \frac{B_0}{B} \frac{\partial f}{\partial u} + \alpha_6 \frac{\partial f}{\partial v_\parallel} \right) \right],
\end{aligned} \tag{33}$$

where $d\vec{z} \equiv d\vec{X} dv_\parallel du$, $d\vec{X} \equiv 2\pi R dR dZ$, and $\mathscr{J} \equiv u B^*_\parallel$. If we integrate Eq. (33) by parts

$$\begin{aligned}\int_{\Omega^{[j,k]}} d\vec{z}\,\mathscr{J}\frac{\partial W f}{\partial t} = &\int_{\Omega^{[j,k]}} d\vec{X} du \left[W\mathscr{J}\left(-\alpha_1 f + \alpha_2 \frac{\partial f}{\partial v_\parallel} + \alpha_5 \frac{\partial f}{\partial u}\right)\right]_{j-1}^{j} \\ &+ \int_{\Omega^{[j,k]}} d\vec{X} dv_\parallel \left[W\mathscr{J}\left(-\alpha_3 f + \alpha_4 \frac{B_0}{B}\frac{\partial f}{\partial u} + \alpha_6 \frac{\partial f}{\partial v_\parallel}\right)\right]_{k-1}^{k} \\ &- \int_{\Omega^{[j,k]}} d\vec{z} \frac{\partial W}{\partial v_\parallel}\left[\mathscr{J}\left(-\alpha_1 f + \alpha_2 \frac{\partial f}{\partial v_\parallel} + \alpha_5 \frac{\partial f}{\partial u}\right)\right] \\ &- \int_{\Omega^{[j,k]}} d\vec{z} \frac{\partial W}{\partial u}\left[\mathscr{J}\left(-\alpha_3 f + \alpha_4 \frac{B_0}{B}\frac{\partial f}{\partial u} + \alpha_6 \frac{\partial f}{\partial v_\parallel}\right)\right]\end{aligned}$$

and do again and then apply Eq. (31), the weighted equation is obtained as

$$\int_{\Omega^{[j,k]}} d\vec{z}\,\mathscr{J}\frac{\partial W f_d^{[j,k]}}{\partial t} = \left[\mathbb{S}_{v_\parallel}^{[j',k]}(W)\right]_{j'=j-1}^{j'=j} + \left[\mathbb{S}_{u}^{[j,k']}(W)\right]_{k'=k-1}^{k'=k} + \mathbb{V}^{[j,k]}(W), \tag{34}$$

where we define the following functions:

$$\mathbb{S}_{v_\parallel}^{[j',k]}(W) \equiv \int_{\Omega_x} d\vec{X} \int_{u_{k'=k-1}}^{u_{k'=k}} du \left[\mathscr{J}\left\{-W\alpha_1 f + W\alpha_2 \frac{\partial f}{\partial v_\parallel} - \frac{\partial W}{\partial v_\parallel}\alpha_2 f - \frac{\partial W}{\partial u}\alpha_6 f\right\}\right]_{v_\parallel = v_{\parallel,j'}}, \tag{35}$$

$$\mathbb{S}_{u}^{[j,k']}(W) \equiv \int_{\Omega_x} d\vec{X} \int_{v_{\parallel,j'=j-1}}^{v_{\parallel,j'=j}} dv_\parallel \left[\mathscr{J}\left\{-W\alpha_3 f + W\frac{B_0}{B}\alpha_4 \frac{\partial f}{\partial u} - \frac{\partial W}{\partial u}\frac{B_0}{B}\alpha_4 f - \frac{\partial W}{\partial v_\parallel}\alpha_5 f\right\}\right]_{u=u_{k'}}, \tag{36}$$

$$\begin{aligned}\mathbb{V}^{[j,k]}(W) \equiv &\int_{\Omega^{[j,k]}} d\vec{z}\left[\frac{\partial W}{\partial v_\parallel}\alpha_1 + \frac{1}{\mathscr{J}}\frac{\partial}{\partial v_\parallel}\left(\frac{\partial W}{\partial v_\parallel}\alpha_2\mathscr{J}\right) + \frac{1}{u}\frac{\partial}{\partial u}\left(\frac{\partial W}{\partial v_\parallel}\alpha_5 u\right)\right. \\ &\left. + \frac{\partial W}{\partial u}\alpha_3 + \frac{1}{u}\frac{\partial}{\partial u}\left(\frac{\partial W}{\partial u}\alpha_4\frac{B_0}{B}u\right) + \frac{1}{\mathscr{J}}\frac{\partial}{\partial v_\parallel}\left(\frac{\partial W}{\partial u}\alpha_6\mathscr{J}\right)\right]\mathscr{J} f_d^{[j,k]}.\end{aligned} \tag{37}$$

$\mathbb{V}^{[j,k]}$ represents the volume integration term and can be evaluated by using quadrature rules. $\mathbb{S}_{v_\parallel}^{[j',k]}$ and $\mathbb{S}_{u}^{[j,k']}$ are surface integration terms at fixed $v_\parallel = v_{\parallel,j'}$ and $u = u_{k'}$, respectively. For the calculation of those surface terms, we mainly follow the method presented in [32] with some minor changes. For completeness, models used in this work for calculation of surface terms are presented in the rest of this section. Although f_d is discontinuous at the boundaries between cells, single-valued functions are required for these surface terms to conserve physical quantities. While there is no single definite way to construct such a single-valued flux, how to model the flux is related to the numerical instability due to the local negativity of f_d. In the DG formalism, it is not trivial to remove the local negativity completely [40]. Also, the local negativity does not necessarily lead to the numerical instability [36]. In [32], it was shown that the upwind flux is effective to maintain the low level of the local negativity and enable numerically stable simulations with Dougherty operator. Therefore, we approximate the advection parts ($\propto \alpha_1, \alpha_3$) of surface terms with the upwind flux. The effectiveness of the upwind flux for controlling the negativity in simulations with the nonlinear RMJ collision operator is more discussed in section 3.2. The diffusion parts ($\propto \alpha_2, \alpha_4, \alpha_5,$ and α_6) of surface terms are evaluated with the continuous probability distribution function reconstructed from f_d of two adjacent cells. More specifically, $\mathbb{S}_{v_\parallel}^{[j',k]}$ is approximated as the

	Basis functions	Domain in the velocity space
$f_d^{[j=j',k]}$	$\zeta_l \in V_X \times \{1, v_\parallel, u, v_\parallel^2, v_\parallel u, u^2\}$	$v_{\parallel,j'=j-1} \le v_\parallel \le v_{\parallel,j'=j}$
$f_d^{[j=j'+1,k]}$	$\zeta_l \in V_X \times \{1, v_\parallel, u, v_\parallel^2, v_\parallel u, u^2\}$	$v_{\parallel,j'=j} \le v_\parallel \le v_{\parallel,j'=j+1}$
$\bar{f}_{v_\parallel}^{[j',k]}$	$\bar{\zeta}_l \in V_X \times \{1, v_\parallel, v_\parallel^2, v_\parallel^3, v_\parallel^4,$ $u, v_\parallel u, v_\parallel^2 u, v_\parallel^3 u, u^2, v_\parallel u^2, v_\parallel^2 u^2\}$	$v_{\parallel,j'=j-1} \le v_\parallel \le v_{\parallel,j'=j+1}$

Table 2: Basis functions and their domain for $f_d^{[j=j',k]}$, $f_d^{[j=j'+1,k]}$ and $\bar{f}_{v_\parallel}^{[j',k]}$.

following model function :

$$\mathbb{S}_{v_\parallel}^{[j',k]}(W) \sim \int_{\Omega_x} d\vec{X} \int_{u_{k'=k-1}}^{u_{k'=k}} du \Big[\mathscr{J} \Big\{ -W\alpha_1 f_{v_\parallel,up}^{[j',k]} + W\alpha_2 G_{v_\parallel}^{[j',k]} - \left(\frac{\partial W}{\partial v_\parallel}\alpha_2 + \frac{\partial W}{\partial u}\alpha_6 \right) F_{v_\parallel}^{[j',k]} \Big\} \Big]_{v_\parallel = v_{\parallel,j'}}. \tag{38}$$

In Eq. (38), different sets of definition for $\left(f_{v_\parallel,up}^{[j',k]}, F_{v_\parallel}^{[j',k]}, G_{v_\parallel}^{[j',k]} \right)$ are used for the inner boundaries and the outermost boundaries, as follows.

1. At the inner boundaries between two cells (i.e., $0 < j' < N_{v_\parallel}$) :

   $f_{v_\parallel,up}^{[j',k]}$ represents the upwind flux which is given as

   $$f_{v_\parallel,up}^{[j',k]} = \begin{cases} f_d^{[j=j',k]} & \text{if } \alpha_1|_{v_\parallel = v_{\parallel,j'}} < 0, \\ f_d^{[j=j'+1,k]} & \text{if } \alpha_1|_{v_\parallel = v_{\parallel,j'}} \ge 0. \end{cases} \tag{39}$$

   $F_{v_\parallel}^{[j',k]}$ stands for the higher-order polynomial $\bar{f}_{v_\parallel}^{[j',k]}$ which is differentiable with respect to $v_\parallel$ at $v_\parallel = v_{\parallel,j'}$. In this work, $\bar{f}_{v_\parallel}^{[j',k]}$ is reconstructed from $f_d^{[j=j',k]}$ and $f_d^{[j=j'+1,k]}$ by the L_2 minimization on the interval $\left[v_{\parallel,j'=j-1}, v_{\parallel,j'=j+1} \right]$. The maximal-order recovery polynomial [32] is used for the basis of $\bar{f}_{v_\parallel}^{[j',k]}$. Basis functions for $f_d^{[j=j',k]}$, $f_d^{[j=j'+1,k]}$ and $\bar{f}_{v_\parallel}^{[j',k]}$ are shown in Table 2, where V_X is the set of spatial basis functions, i.e., $\{R^{l_1} Z^{l_2} : l_1 + l_2 \le 2, l_i \in \mathbb{Z}_{\ge 0}\}$. Coefficients for $\bar{f}_{v_\parallel}^{[j',k]}$ can be evaluated from

   $$\int_{\Omega_x} d\vec{X} \int_{u_{k'=k-1}}^{u_{k'=k}} du \int_{v_{\parallel,j'=j-1}}^{v_{\parallel,j'=j+1}} dv_\parallel \mathscr{J} \bar{\zeta}_l \left[\bar{f}_{v_\parallel}^{[j',k]} - \left(f_d^{[j=j',k]} + f_d^{[j=j'+1,k]} \right) \right] = 0, \tag{40}$$

   where $\bar{\zeta}_l$ is a basis function for $\bar{f}_{v_\parallel}^{[j',k]}$ with $1 \le l \le 12$. More detailed information about this reconstruction can be found in [32]. Also, $G_{v_\parallel}^{[j',k]}$ is defined as $\partial \bar{f}_{v_\parallel}^{[j',k]} / \partial v_\parallel$.

2. At the outermost boundaries (i.e., $j' = 0$ or $N_{v_\parallel}$) :

   $f_{v_\parallel,up}^{[j',k]}$ and $G_{v_\parallel}^{[j',k]}$ are set to zero, which effectively prevents any net particle flux across the outermost boundaries as shown in the subsection 2.3. On the other hand, unphysical accumulation of particles is observed when $F_{v_\parallel}^{[j',k]}$ are set to zero at the outermost boundaries. To avoid this numerical difficulty, we use $F_{v_\parallel}^{[j'=0,k]} = f_d^{[j=1,k]}$ and $F_{v_\parallel}^{[j'=N_{v_\parallel},k]} = f_d^{[j=N_{v_\parallel},k]}$, as done in [32]. Even though those terms do not affect the net particle conservation, they can induce the finite momentum and energy flux across the outermost boundaries.

Similarly, $\mathbb{S}_u^{[j,k']}$ is approximated as

$$\mathbb{S}_u^{[j,k']}(W) \sim \int_{\Omega_x} d\vec{X} \int_{v_{\parallel,j'=j-1}}^{v_{\parallel,j'=j}} dv_\parallel \left[\mathscr{J} \left\{ -W\alpha_3 f_{u,up}^{[j,k']} + W\frac{B_0}{B}\alpha_4 G_u^{[j,k']} - \left(\frac{\partial W}{\partial u}\frac{B_0}{B}\alpha_4 + \frac{\partial W}{\partial v_\parallel}\alpha_5 \right) F_u^{[j,k']} \right\} \right]_{u=u_{k'}}, \tag{41}$$

where we use the following definitions:

$$f_{u,up}^{[j,k']} = \begin{cases} f_d^{[j,k=k']} & \text{if } 0 < k' < N_u \text{ and } \alpha_3|_{u=u_{k'}} < 0, \\ f_d^{[j,k=k'+1]} & \text{if } 0 < k' < N_u \text{ and } \alpha_3|_{u=u_{k'}} \geq 0. \\ 0 & \text{if } k' = 0 \text{ or } N_u, \end{cases} \tag{42}$$

$$\left(F_u^{[j,k']}, G_u^{[j,k']}\right) = \begin{cases} \left(\bar{f}_u^{[j,k']}, \partial \bar{f}_u^{[j,k']}/\partial u\right) & \text{if } 0 < k' < N_u, \\ \left(f_d^{[j,k=1]}, 0\right) & \text{if } k' = 0, \\ \left(f_d^{[j,k=N_u]}, 0\right) & \text{if } k' = N_u. \end{cases} \tag{43}$$

Here, $\bar{f}_u^{[j,k']}$ is the higher-order polynomial reconstructed from $f_d^{[j,k=k']}$ and $f_d^{[j,k=k'+1]}$ on the interval $u = [u_{k'=k-1}, u_{k'=k+1}]$. If we set $W = \zeta_l^{[j,k]}$ and substitute Eq. (32) into Eq. (34), the weight evolution equations of $\hat{f}_{l'}^{[j,k]}(t)$ is obtained as

$$\sum_{l'} M_{ll'}^{[j,k]} \frac{\partial \hat{f}_{l'}^{[j,k]}}{\partial t} = \left[\mathbb{S}_{v_\parallel}^{[j',k]}\left(\zeta_l^{[j,k]}\right)\right]_{j'=j-1}^{j'=j} + \left[\mathbb{S}_u^{[j,k']}\left(\zeta_l^{[j,k]}\right)\right]_{k'=k-1}^{k'=k} + \mathbb{V}^{[j,k]}\left(\zeta_l^{[j,k]}\right), \tag{44}$$

where $M_{ll'}^{[j,k]} \equiv \int_{\Omega^{[j,k]}} d\vec{z}\, \mathscr{J}\, \zeta_l^{[j,k]} \zeta_{l'}^{[j,k]}$. For the temporal discretization, a third-order SSP (Strong Stability Preserving) Runge-Kutta method [41] is used. As shown in [32], the numerical stability of DG collision operator with SSP is strongly affected by the grid size and the order of basis functions. Numerical estimation for the maximum time step size of Eq. (44) is given in the section 3.3.

2.3 Conservation of physical quantities

Since one of principal objectives in this work is the development of collision operators for gyrokinetic simulations, it is important to ensure that the operators satisfies the conservation of relevant physical variables. We focus on 3 major conserved moments given as

$$M_0 = \sum_{j,k} \int_{\Omega^{[j,k]}} d\vec{z}\, \mathscr{J}\, f_d^{[j,k]}, \tag{45}$$

$$M_1 = \sum_{j,k} \int_{\Omega^{[j,k]}} d\vec{z} v_\parallel\, \mathscr{J}\, f_d^{[j,k]}, \tag{46}$$

$$M_2 = \sum_{j,k} \int_{\Omega^{[j,k]}} d\vec{z} E\, \mathscr{J}\, f_d^{[j,k]}, \tag{47}$$

where E is defined as $\frac{1}{2}(v_\parallel^2 + u^2 B/B_0)$. From these moments, the parallel fluid velocity $U_\parallel$ and the thermal velocity v_T can be obtained as

$$U_\parallel = \frac{M_1}{M_0}, \tag{48}$$

$$v_T^2 = \frac{2}{3}\left(\frac{M_2}{M_0} - \frac{1}{2}U_\parallel^2\right). \tag{49}$$

M_0 of Eq. (45) represents the total number of particles and $\partial M_0/\partial t$ can be evaluated from Eq. (34) with $W = 1$ as

$$\begin{aligned}\frac{\partial M_0}{\partial t} &= \sum_{j,k}\int_{\Omega^{[j,k]}} d\vec{z}\,\mathscr{J}\,\frac{\partial}{\partial t}\left[f_d^{[j,k]}\right] = \sum_k \left[\mathbb{S}_{v_\parallel}^{[j',k]}(1)\right]_{j'=0}^{j'=N_{v_\parallel}} + \sum_j \left[\mathbb{S}_u^{[j,k']}(1)\right]_{k'=0}^{k'=N_u} \\ &= \int_{\Omega_x} d\vec{X}\int_0^{u_{\max}} du\left[\left\{-\mathscr{J}\,\alpha_1 f_{v_\parallel,up}^{[j',k]} + \mathscr{J}\,\alpha_2 G_{v_\parallel}^{[j',k]}\right\}_{v_\parallel = v_{\parallel,j'}}\right]_{j'=0}^{j'=N_{v_\parallel}} \\ &+ \int_{\Omega_x} d\vec{X}\int_{v_{\parallel,\min}}^{v_{\parallel,\max}} dv_\parallel\left[\left\{-\mathscr{J}\,\alpha_3 f_{u,up}^{[j,k']} + \mathscr{J}\,\frac{B_0}{B}\alpha_4 G_u^{[j,k']}\right\}_{u=u_{k'}}\right]_{k'=0}^{k'=N_u} = 0,\end{aligned} \tag{50}$$

since $f_{v_\parallel,up}^{[j',k]}$, $f_{u,up}^{[j,k']}$, $G_{v_\parallel}^{[j',k]}$ and $G_u^{[j,k']}$ are set to zero at the outermost boundaries. Therefore, the particle number conservation is satisfied with any choice of α_s. The momentum conservation constraint, i.e., $\partial M_1/\partial t = 0$, can be obtained from Eq. (34) with $W = v_\parallel$ as

$$\begin{aligned}\frac{\partial M_1}{\partial t} &= \sum_{j,k}\int_{\Omega^{[j,k]}} d\vec{z}\,\mathscr{J}\,\frac{\partial}{\partial t}\left[v_\parallel f_d^{[j,k]}\right] \\ &= \sum_k \left[\mathbb{S}_{v_\parallel}^{[j',k]}(v_\parallel)\right]_{j'=0}^{j'=N_{v_\parallel}} + \sum_{j,k}\mathbb{V}^{[j,k]}\left(v_\parallel\right) = 0.\end{aligned} \tag{51}$$

Similarly, the energy conservation constraint, i.e., $\partial M_2/\partial t = 0$, can be formulated from Eq. (34) with $W = E$ as

$$\begin{aligned}\frac{\partial M_2}{\partial t} &= \sum_{j,k}\int_{\Omega^{[j,k]}} d\vec{z}\,\mathscr{J}\,\frac{\partial}{\partial t}\left[E f_d^{[j,k]}\right] \\ &= \sum_k \left[\mathbb{S}_{v_\parallel}^{[j',k]}(E)\right]_{j'=0}^{j'=N_{v_\parallel}} + \sum_j \left[\mathbb{S}_u^{[j,k']}(E)\right]_{k'=0}^{k'=N_u} + \sum_{j,k}\mathbb{V}^{[j,k]}(E) = 0.\end{aligned} \tag{52}$$

Since it is not guaranteed that Eqs. (51) and (52) are automatically satisfied, additional numerical operations are required for the conservation of M_1 and M_2. In the following subsections, two numerical conservation methods used in this work are presented.

2.3.1 Simple advection-diffusion model

With the coefficients for the Dougherty operator in Table 1, the conservation constraints, Eqs. (51) and (52), can be written as

$$\frac{\partial M_1}{\partial t} = \sum_k \left[\mathbb{S}_{v_\parallel}^{[j',k]}(v_\parallel)\right]_{j'=0}^{j'=N_{v_\parallel}} + \bar{\nu} v_T^2 \sum_{j,k} \int_{\Omega^{[j,k]}} d\vec{z} \frac{\partial \mathscr{J}}{\partial v_\parallel} f_d^{[j,k]} - \bar{\nu}\left[M_1 - U_\parallel M_0\right] = 0, \tag{53}$$

$$\frac{\partial M_2}{\partial t} = \sum_k \left[\mathbb{S}_{v_\parallel}^{[j',k]}(E)\right]_{j'=0}^{j'=N_{v_\parallel}} + \sum_j \left[\mathbb{S}_u^{[j,k']}(E)\right]_{k'=0}^{k'=N_u} + \bar{\nu} v_T^2 \sum_{j,k} \int_{\Omega^{[j,k]}} d\vec{z} \left[v_\parallel \frac{\partial \mathscr{J}}{\partial v_\parallel}\right] f_d^{[j,k]} + 2\bar{\nu} M_0 \left[\frac{3}{2} v_T^2 - \frac{M_2}{M_0} + \frac{1}{2} U_\parallel \frac{M_1}{M_0}\right] = 0. \tag{54}$$

If we assume that $\partial \mathscr{J} / \partial v_\parallel$ and the outermost boundary terms can be neglected, Eqs. (53) and (54) can be simplified as

$$\frac{\partial M_1}{\partial t} = -\bar{\nu}\left[M_1 - U_\parallel M_0\right] = 0, \tag{55}$$

$$\frac{\partial M_2}{\partial t} = 2\bar{\nu} M_0 \left[\frac{3}{2} v_T^2 - \frac{M_2}{M_0} + \frac{1}{2} U_\parallel \frac{M_1}{M_0}\right] = 0, \tag{56}$$

which are well satisfied if $U_\parallel$ and v_T^2 are given as Eqs. (48) and (49). But, if $\partial \mathscr{J} / \partial v_\parallel$ and the outermost boundary terms of Eqs. (53) and (54) have finite values, additional operations are required to satisfy the momentum and energy conservation. In [32], $U_\parallel$ and v_T^2 are redefined from Eqs. (53) and (54) to satisfy the conservation automatically. In this work, instead of modifying the definitions for $U_\parallel$ and v_T^2, a simple advection-diffusion operator L_A is introduced as

$$\partial f / \partial t = C(f) + L_A(f), \tag{57}$$

where

$$L_A(f) \equiv -\beta_1 \frac{1}{B_\parallel^*} \frac{\partial}{\partial v_\parallel}\left(B_\parallel^* f\right) + \beta_2 \left[\frac{1}{B_\parallel^*} \frac{\partial}{\partial v_\parallel}\left(B_\parallel^* \frac{\partial f}{\partial v_\parallel}\right) + \frac{1}{u} \frac{\partial}{\partial u}\left(u \frac{B_0}{B} \frac{\partial f}{\partial u}\right)\right]. \tag{58}$$

Here, β_1 and β_2 are free parameters used to ensure the conservation. This kind of methods introducing free parameters has been widely used for the conservation property of collision operators. For instance, iterative conservation approaches for particle-in-cell methods and finite difference methods (FDMs) are suggested in [42] and in [43], respectively, and references therein. In addition, a non-iterative method is introduced in [44]. Also, a more sophisticated model including multi-species cases is developed for finite volume methods (FVMs) in [27]. The 1st term of the right hand side (RHS) of Eq. (58) is an advection operator in $v_\parallel$ direction and the 2nd term of RHS is a diffusion operator. Since L_A is in the divergence form, the particle conservation is affected little by introducing L_A. With Eq. (57), the weighted equation Eq. (34) is modified as

$$\int_{\Omega^{[j,k]}} d\vec{z} \frac{\partial W \mathscr{J} f_d^{[j,k]}}{\partial t} = \int_{\Omega^{[j,k]}} d\vec{z} W \mathscr{J} \left[C(f_d^{[j,k]}) + L_A(f_d^{[j,k]})\right] = \left[\mathbb{S}_{v_\parallel}^{[j',k]}(W)\right]_{j'=j-1}^{j'=j} + \left[\mathbb{S}_u^{[j,k']}(W)\right]_{k'=k-1}^{k'=k} + \mathbb{V}^{[j,k]}(W) + \sum_{n=1}^{2} \beta_n \mathbb{L}_{A,n}^{[j,k]}(W), \tag{59}$$

where

$$\mathbb{L}_{A,1}^{[j,k]}(W) = \int_{\Omega_x} d\vec{X} \int_{u_{k'=k-1}}^{u_{k'=k}} du \left[\left\{ -\mathscr{J} W f_{v_\parallel,up}^{[j',k]} \right\}_{v_\parallel = v_{\parallel,j'}} \right]_{j'=j-1}^{j'=j} + \int_{\Omega^{[j,k]}} d\vec{z} \frac{\partial W}{\partial v_\parallel} \mathscr{J} f_d^{[j,k]}, \tag{60}$$

$$\begin{aligned}\mathbb{L}_{A,2}^{[j,k]}(W) = &\int_{\Omega_x} d\vec{X} \int_{u_{k'=k-1}}^{u_{k'=k}} du \left[\left\{ \mathscr{J} W G_{v_\parallel}^{[j',k]} - \mathscr{J} \frac{\partial W}{\partial v_\parallel} F_{v_\parallel}^{[j',k]} \right\}_{v_\parallel = v_{\parallel,j'}} \right]_{j'=j-1}^{j'=j} \\ &+ \int_{\Omega_x} d\vec{X} \int_{v_{\parallel,j'=j-1}}^{v_{\parallel,j'=j}} dv_\parallel \mathscr{J} \left[\left\{ W \frac{B_0}{B} G_u^{[j,k']} - \frac{\partial W}{\partial u} \frac{B_0}{B} F_u^{[j,k']} \right\}_{u=u_{k'}} \right]_{k'=k-1}^{k'=k} \\ &+ \int_{\Omega^{[j,k]}} d\vec{z} \left[\frac{1}{\mathscr{J}} \frac{\partial}{\partial v_\parallel} \left(\frac{\partial W}{\partial v_\parallel} \mathscr{J} \right) + \frac{1}{u} \frac{\partial}{\partial u} \left(\frac{\partial W}{\partial u} \frac{B_0}{B} u \right) \right] \mathscr{J} f_d^{[j,k]}.\end{aligned} \tag{61}$$

With Eq. (59), $\partial M_1/\partial t = 0$ and $\partial M_2/\partial t = 0$ can be written as

$$\frac{\partial M_1}{\partial t} = \sum_k \left[\mathbb{S}_{v_\parallel}^{[j',k]}(v_\parallel) \right]_{j'=0}^{j'=N_{v_\parallel}} + \sum_{j,k} \mathbb{V}^{[j,k]}(v_\parallel) + \sum_{j,k} \sum_{n=1}^{2} \beta_n \mathbb{L}_{A,n}^{[j,k]}(v_\parallel) = 0, \tag{62}$$

$$\begin{aligned}\frac{\partial M_2}{\partial t} = &\sum_k \left[\mathbb{S}_{v_\parallel}^{[j',k]}(E) \right]_{j'=0}^{j'=N_{v_\parallel}} + \sum_j \left[\mathbb{S}_u^{[j,k']}(E) \right]_{k'=0}^{k'=N_u} + \sum_{j,k} \mathbb{V}^{[j,k]}(E) \\ &+ \sum_{j,k} \sum_{n=1}^{2} \beta_n \mathbb{L}_{A,n}^{[j,k]}(E) = 0.\end{aligned} \tag{63}$$

Once β_1 and β_2 are calculated from Eqs. (62) and (63), the weight evolution equations are obtained from Eq. (59) with $W = \zeta_l^{[j,k]}$ as

$$\begin{aligned}\sum_{l'} M_{ll'}^{[j,k]} \frac{\partial \hat{f}_{l'}^{[j,k]}}{\partial t} = &\left[\mathbb{S}_{v_\parallel}^{[j',k]} \left(\zeta_l^{[j,k]} \right) \right]_{j'=j-1}^{j'=j} + \left[\mathbb{S}_u^{[j,k']} \left(\zeta_l^{[j,k]} \right) \right]_{k'=k-1}^{k'=k} \\ &+ \mathbb{V}^{[j,k]} \left(\zeta_l^{[j,k]} \right) + \sum_{n=1}^{2} \beta_n \mathbb{L}_{A,n}^{[j,k]} \left(\zeta_l^{[j,k]} \right).\end{aligned} \tag{64}$$

Although the Dougherty model is chosen as an example in this section, the L_A operator is also employed to ensure the conservation properties of the nonlinear collision operator in the rest of this thesis, if not explicitly stated otherwise.

2.3.2 Linearized field particle collision model

Unlike the Dougherty model, the test particle collision does not satisfy Eqs. (51) and (52), even if $\partial \mathscr{J}/\partial v_\parallel$ and the outermost boundary terms are neglected. This is partially because the field particle collision part is not properly accounted for. Therefore, we implement the linearized field particle collision L_F for the test particle collision, as well as L_A. The functional form of L_F used in this work is given as [42, 43]

$$L_F \equiv \sum_{n=1}^{3} \gamma_n \sum_{j,k} L_{F,n}^{[j,k]}, \tag{65}$$

where

$$L_{F,1}^{[j,k]} = f_{M,d}^{[j,k]}, \tag{66}$$

$$L_{F,2}^{[j,k]} = \left(v_\parallel - U_\parallel\right) y^{-3/2} \phi(y) f_{M,d}^{[j,k]}, \tag{67}$$

$$L_{F,3}^{[j,k]} = y^{-1/2} \left(\phi(y) - \frac{d\phi(y)}{dy}\right) f_{M,d}^{[j,k]}, \tag{68}$$

$$y = \frac{\left(v_\parallel - U_\parallel\right)^2 + u^2 B/B_0}{2v_T^2}. \tag{69}$$

Here, $\phi(y) = \frac{2}{\sqrt{\pi}} \int_0^y e^{-t}\sqrt{t}dt$ is the Maxwellian integral. $f_{M,d}^{[j,k]}$ is the Maxwellian function discretized with the DG basis $\{\zeta^{[j,k]}\}$ and recalculated at each collision time step. Also, γ_n's are free parameters used to enforce the conservation, as in the case of L_A. With L_F, the weighted equation, Eq. (34), can be written as

$$\int_{\Omega^{[j,k]}} d\vec{z} \frac{\partial W \mathscr{J} f_d^{[j,k]}}{\partial t} = \int_{\Omega^{[j,k]}} d\vec{z} W \mathscr{J} \left[C(f_d^{[j,k]})\right] + \sum_{n=1}^{3} \gamma_n \mathbb{L}_{F,n}^{[j,k]}(W), \tag{70}$$

where $\mathbb{L}_{F,n}^{[j,k]}(W) = \int_{\Omega^{[j,k]}} d\vec{z} \left[W \mathscr{J} L_{F,n}^{[j,k]}\right]$. From Eq. (70), the constraints for conservation are given as follows.

$$\frac{\partial M_p}{\partial t} = \int_{\Omega^{[j,k]}} d\vec{z} \frac{\partial w_p \mathscr{J} f_d^{[j,k]}}{\partial t} = \int_{\Omega^{[j,k]}} d\vec{z} w_p \mathscr{J} \left[C(f_d^{[j,k]})\right] + \sum_{n=1}^{3} \gamma_n \mathbb{L}_{F,n}^{[j,k]}(w_p) = 0, \tag{71}$$

where $p \in \{0,1,2\}$ and $[w_0, w_1, w_2] = [1, v_\parallel, E]$. Note that a constraint for the particle number conservation, i.e., $\partial M_0/\partial t = 0$, is included in Eq. (71), since L_F is not in the divergence form of f. Unlike the case of L_A introduced in the previous section, the enforcement of $\partial M_0/\partial t = 0$ is important for L_F to guarantee the numerical stability of simulations. Once γ_n's are calculated from Eq. (71), the weight evolution for $f_d^{[j,k]}$ can be calculated from Eq. (70) with $W = \zeta_l^{[j,k]}$. To distinguish [the test particle collision + L_F] from [the test particle collision + L_A], we refer the former as "Linearized collision operator", while the latter is just called as "Test particle collision operator" in the rest of this thesis.

2.4 FEM solver for the Rosenbluth potential

In this section, the method used to calculate the Rosenbluth potentials is presented. With $\left(v_{\parallel o}, v_{\perp o}\right) \sim \left(v_\parallel, u\sqrt{B/B_0}\right)$, Eqs. (16) and (17) can be approximated as

$$f = -\frac{1}{u}\frac{\partial}{\partial u}\left[\frac{B_0}{B} u \frac{\partial h}{\partial u}\right] - \frac{\partial^2 h}{\partial v_\parallel^2}, \tag{72}$$

$$h = \frac{1}{u}\frac{\partial}{\partial u}\left[\frac{B_0}{B} u \frac{\partial g}{\partial u}\right] + \frac{\partial^2 g}{\partial v_\parallel^2}. \tag{73}$$

Since derivatives of h and g are required for the collision operator, the finite element method (FEM) with continuous basis functions is used for h and g. In this case, the maximum order of the basis functions

should be higher enough to deal with the derivative order required for coefficients α_i's in Eqs. (35)-(37). For the RMJ operator, Eq. (37) can be written as

$$\mathbb{V}^{[j,k]}(W) = \Gamma \int_{\Omega^{[j,k]}} d\vec{z} \left[\frac{\partial W}{\partial v_\parallel}\frac{\partial h}{\partial v_\parallel} + \frac{1}{\mathscr{J}}\frac{\partial}{\partial v_\parallel}\left(\frac{\partial W}{\partial v_\parallel}\frac{\partial^2 g}{\partial v_\parallel^2}\mathscr{J}\right) + \frac{B_0}{B}\frac{1}{u}\frac{\partial}{\partial u}\left(\frac{\partial W}{\partial v_\parallel}\frac{\partial^2 g}{\partial v_\parallel \partial u}u\right) + \frac{B_0}{B}\frac{\partial W}{\partial u}\frac{\partial h}{\partial u} + \frac{B_0^2}{B^2}\frac{1}{u}\frac{\partial}{\partial u}\left(\frac{\partial W}{\partial u}\frac{\partial^2 g}{\partial u^2}u\right) + \frac{B_0}{B}\frac{1}{\mathscr{J}}\frac{\partial}{\partial v_\parallel}\left(\frac{\partial W}{\partial u}\frac{\partial^2 g}{\partial v_\parallel \partial u}\mathscr{J}\right)\right] \mathscr{J} f_d^{[j,k]}, \tag{74}$$

which contains the third order derivatives of g such as $\partial^3 g/\partial v_\parallel^3$. When we replace those third order derivatives of g with the first order derivatives of h, Eq. (74) can be rearranged as

$$\mathbb{V}^{[j,k]}(W) = \Gamma \int_{\Omega^{[j,k]}} d\vec{z} \left[\left\{ 2\frac{\partial h}{\partial v_\parallel} + \frac{\partial^2 g}{\partial v_\parallel^2}\frac{1}{\mathscr{J}}\frac{\partial \mathscr{J}}{\partial v_\parallel} \right\}\frac{\partial W}{\partial v_\parallel} + \frac{\partial^2 g}{\partial v_\parallel^2}\frac{\partial^2 W}{\partial v_\parallel^2} + 2\frac{B_0}{B}\frac{\partial^2 g}{\partial v_\parallel \partial u}\frac{\partial^2 W}{\partial v_\parallel \partial u} + \frac{B_0}{B}\left\{ 2\frac{\partial h}{\partial u} + \frac{\partial^2 g}{\partial v_\parallel \partial u}\frac{1}{\mathscr{J}}\frac{\partial \mathscr{J}}{\partial v_\parallel} + \frac{B_0}{B}\frac{1}{u^2}\frac{\partial g}{\partial u} \right\}\frac{\partial W}{\partial u} + \left(\frac{B_0}{B}\right)^2 \frac{\partial^2 g}{\partial u^2}\frac{\partial^2 W}{\partial u^2} \right] \mathscr{J} f_d^{[j,k]}. \tag{75}$$

The detail of derivation of Eq. (75) is given in Appendix B. In [45], (h, g) are split into Maxwellian and non-Maxwellian parts to preserve the Maxwellian distribution function exactly at the equilibrium. Similarly, we split (h, g) into the equilibrium parts (h_M, g_M) and the residual parts $(\delta h, \delta g)$ in this work. Here, (h_M, g_M) are the analytic solutions of following equations.

$$f_M = -\frac{1}{u}\frac{\partial}{\partial u}\left[\frac{B_0}{B}u\frac{\partial h_M}{\partial u}\right] - \frac{\partial^2 h_M}{\partial v_\parallel^2}, \tag{76}$$

$$h_M = \frac{1}{u}\frac{\partial}{\partial u}\left[\frac{B_0}{B}u\frac{\partial g_M}{\partial u}\right] + \frac{\partial^2 g_M}{\partial v_\parallel^2}. \tag{77}$$

(h_M, g_M) are introduced to improve the numerical resolution when f is close to f_M and their specific forms are given in Eqs. (A.13) and (A.14). The effect of including (h_M, g_M) is demonstrated in the section 3.1. Since the maximum derivative order of Eq. (75) is the second order, cubic B-splines are chosen as basis functions for $(\delta h, \delta g)$. With those basis functions, δh and δg for each spatial mesh Ω_x can be expressed as follows.

$$\delta h(\vec{z}) = \sum_{i_1=-1}^{N_{v_\parallel}+1} \sum_{i_2=-1}^{N_u+1} h_i \Lambda_i(v_\parallel, u), \tag{78}$$

$$\delta g(\vec{z}) = \sum_{i_1=-1}^{N_{v_\parallel}+1} \sum_{i_2=-1}^{N_u+1} g_i \Lambda_i(v_\parallel, u), \tag{79}$$

where $i \equiv [i_1, i_2]$ is a set of indexes for the basis $\Lambda_i(v_\parallel, u) \equiv \Upsilon_{v_\parallel, i_1}(v_\parallel)\Upsilon_{u,i_2}(u)$. Here, $\Upsilon_{v_\parallel, i_1}(v_\parallel)$ and $\Upsilon_{u,i_2}(u)$ are cubic B-spline functions centered at $v_\parallel = v_{\parallel, j'=i_1}$ and $u = u_{k'=i_2}$, respectively. In Eqs. (78) and (79), we ignored the spatial variation of δh and δg within a single cell to avoid numerical instability which can occur where f_d becomes locally negative within the spatial cell. If we take $\int d\vec{z}\frac{2\pi B}{B_0} Ru\Lambda_{i'} \times$ to [Eq. (72) $-$ Eq. (76)] and integrate it by parts, the following equation is obtained.

$$\int \frac{2\pi B}{B_0} Rud\vec{z}\Lambda_{i'}(f - f_M) = -V \int dv_\parallel u\Lambda_{i'} \frac{\partial \delta h}{\partial u}\bigg|_{u_{k'=i_2'-2}}^{u_{k'=i_2'+2}} - V_B \int duu\Lambda_{i'} \frac{\partial \delta h}{\partial v_\parallel}\bigg|_{v_{\parallel, j'=i_1'-2}}^{v_{\parallel, j'=i_1'+2}} + V \int dv_\parallel duu \frac{\partial \Lambda_{i'}}{\partial u}\frac{\partial \delta h}{\partial u} + V_B \int dv_\parallel duu \frac{\partial \Lambda_{i'}}{\partial v_\parallel}\frac{\partial \delta h}{\partial v_\parallel}, \tag{80}$$

where $V \equiv \int_{\Omega_x} d\vec{X} 2\pi R$ and $V_B \equiv \int_{\Omega_x} d\vec{X} 2\pi R \frac{B}{B_0}$. With Eqs. (31), (78) and (80), a set of linear equations for h_i can be expressed as

$$\sum_i N_{i'i} h_i = \sum_{j,k,l} \Theta_{i'l}^{[j,k]} (\hat{f}_l^{[j,k]} - \hat{f}_{M,l}^{[j,k]}). \tag{81}$$

where

$$\begin{aligned} N_{i'i} = &-V \int dv_\parallel u \Lambda_{i'} \frac{\partial \Lambda_i}{\partial u} \Big|_{u_{k'=i'_2-2}}^{u_{k'=i'_2+2}} - V_B \int du u \Lambda_{i'} \frac{\partial \Lambda_i}{\partial v_\parallel} \Big|_{v_{\parallel,j'=i'_1-2}}^{v_{\parallel,j'=i'_1+2}} \\ &+ V \int dv_\parallel du u \frac{\partial \Lambda_{i'}}{\partial u} \frac{\partial \Lambda_i}{\partial u} + V_B \int dv_\parallel du u \frac{\partial \Lambda_{i'}}{\partial v_\parallel} \frac{\partial \Lambda_i}{\partial v_\parallel}, \\ \Theta_{i'l}^{[j,k]} = &\int \frac{2\pi B}{B_0} R u d\vec{z} \Lambda_{i'} \zeta_l^{[j,k]}. \end{aligned}$$

Here $\hat{f}_{M,l}^{[j,k]}$ is a coefficient of the discretized Maxwellian function $f_{M,d}^{[j,k]}$. Similarly, $\int d\vec{z} \frac{2\pi B}{B_0} R u \Lambda_{i'} \times$ [Eq. (73) $-$ Eq. (77)] can be written as

$$\sum_i N_{i'i} g_i = \sum_i \Xi_{i'i} h_i, \tag{82}$$

where

$$\Xi_{i'i} = -\int \frac{2\pi B}{B_0} R u d\vec{z} \Lambda_{i'} \Lambda_i.$$

Boundary conditions required for Eqs. (81) and (82) are calculated at the outermost vertices $(v_\parallel, u) = (v_{\parallel,C}, u_C)$ as [25]

$$\begin{aligned} \delta h(v_{\parallel,C}, u_C) &= \frac{2}{V} \sum_{j,k} \int_{\Omega^{[j,k]}} d\vec{z} R u \frac{B}{B_0} \frac{\delta f_d^{[j,k]}(v_\parallel, u) K[\bar{k}]}{\mathbb{D}}, \\ \delta g(v_{\parallel,C}, u_C) &= \frac{1}{V} \sum_{j,k} \int_{\Omega^{[j,k]}} d\vec{z} R u \frac{B}{B_0} \delta f_d^{[j,k]}(v_\parallel, u) E[\bar{k}] \mathbb{D}, \end{aligned} \tag{83}$$

where

$$\begin{aligned} \delta f_d^{[j,k]} &= f_d^{[j,k]} - f_{M,d}^{[j,k]}, \\ \mathbb{D} &= \sqrt{\frac{B}{B_0}(u_C + u)^2 + (v_{\parallel,C} - v_\parallel)^2}, \\ \bar{k} &= \frac{1}{\mathbb{D}} \sqrt{4 u u_C B / B_0}. \end{aligned}$$

Here, $K[\bar{k}]$ and $E[\bar{k}]$ are the complete elliptic integrals of the first kind and the second kind, respectively. At $u = 0$, Neumann boundary conditions, $\partial \delta h / \partial u = \partial \delta g / \partial u = 0$, are used.

III Numerical properties of the developed model

3.1 Numerical convergence test with the initially loaded Maxwellian distribution function

In this subsection, we present how accurately the developed collision operators can maintain the initially loaded Maxwellian distribution function f_M. The velocity domain for the test is $v_\parallel \in [-10v_T, 10v_T]$ and $u \in [0, 10v_T]$. The explicit time step is set as $\Delta t = 0.001\tau$, where τ is the ion self-collision time which is defined as the inverse of $\bar{\nu}$ in Eq. (26). To measure the deviation of f from the initial f_M, the residual of $C(f_M)$ is defined as

$$L_2^{\Delta v} \equiv \sqrt{\sum_{j,k} \int_{\Omega^{[j,k]}} d\vec{z}\, \mathscr{J} \left[f_d^{[j,k]}(t = 50\tau) - f_d^{[j,k]}(t = 0) \right]^2}. \tag{84}$$

Results with various grid size Δv are shown in Fig. 3. Here, Δv is a grid size of each velocity cell, i.e., $\Delta v_\parallel = \Delta u = \Delta v$ where $\Delta v_\parallel$ (Δu) is the grid size in the $v_\parallel$ (u) direction. The overall convergence rate is approximately $(\Delta v)^{1.6}$ which is a slightly degraded result, compared to the second-order convergence reported for the finite volume method (FVM) case [27]. It is noticeable that $L_2^{\Delta v}$ of the Dougherty operator (the blue circle symbols) is an order of magnitude smaller than values from the other operators. This difference is closely related to the cross-diffusion terms (e.g., $\partial^2/\partial v_\parallel \partial u$) which are not included in the Dougherty model. For instance, if we artificially remove the cross-diffusion terms in the linearized collision model, $L_2^{\Delta v}$'s from the linearized collision model (the green asterisk symbols) are at the same level of $L_2^{\Delta v}$'s from the Dougherty model. While the specific choice of velocity space grids or the basis functions might change the results, the detailed study on this issue is not in the scope of this work. The linearized (the red cross symbols) and the nonlinear operators (the black square symbols) show almost identical results, which is expected from that the α_i's from h_M and g_M are identical to α_i's for the test particle collision. To demonstrate the effect of utilizing h_M and g_M, we test a modified nonlinear collision model in which the total h and g are described by the cubic spline basis functions only, without h_M and g_M. As shown in Fig. 3, the nonlinear case without h_M and g_M (the magenta diamond symbols) shows higher $L_2^{\Delta v}$ than the values from the case with h_M and g_M (the black square symbols). This result indicates that the resolution of nonlinear collision operators can be improved by using h_M and g_M, especially when f is close to f_M. As mentioned in the preceding subsection 2.4, the separation of (h_M, g_M) from (h, g) is previously studied in [45]. In [45], the advective and diffusive flux are also modified to exactly preserve f_M at the equilibrium. Although the flux modification is not implemented in this work, overall effects of introducing (h_M, g_M) are consistent to the results presented in [45].

The computing time for each collision operator is summarized in Table 3. Currently, the code [35] in which collision operators of this work are implemented is based on the C++ language and supplemented by Intel MKL libraries. While the code is MPI-parallelized for multi-core simulations, a single CPU is used for this benchmark, since each spatial cell is assigned to a single CPU core and the velocity space is not MPI-parallelized. The model of CPU used in this test is the Intel Xeon Platinum 8260. Two cases with different velocity dimensions, i.e., $[N_{v_\parallel}, N_u] = [20, 10]$ and $[60, 30]$, are tested for this

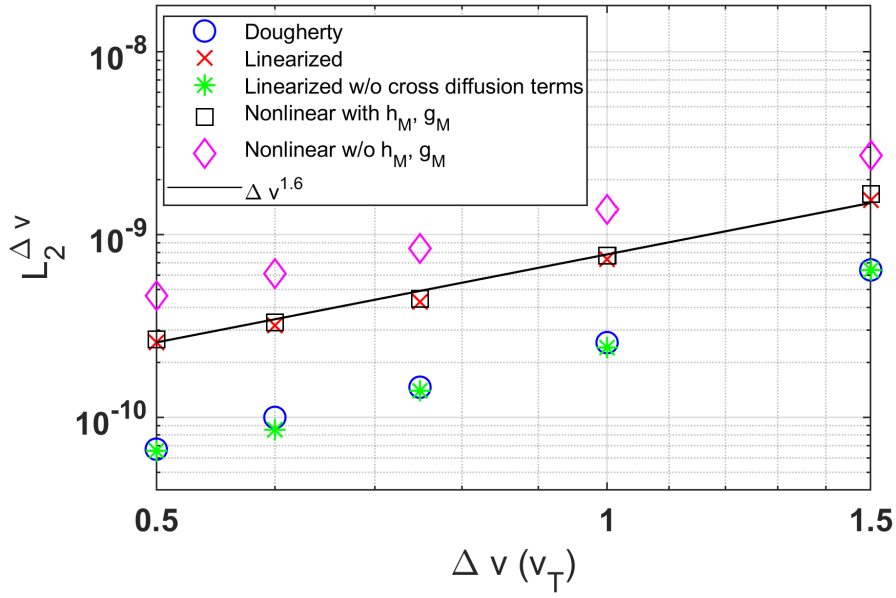

Figure 3: The residual of $C(f_M)$ with varying grid sizes. Δv is the grid size of each velocity cell for both of $v_\parallel$ and u directions.

benchmark. In Table 3, numbers without parentheses represent $[N_{v_\parallel}, N_u] = [20, 10]$ case, while numbers inside parentheses are results with $[N_{v_\parallel}, N_u] = [60, 30]$. 'Boundary conditions for δh and δg' is the time needed to calculate the boundary conditions for the Rosenbluth potentials, i.e., Eq. (83). For this part of calculation, the ratio between the required times from $[N_{v_\parallel}, N_u] = [60, 30]$ and $[N_{v_\parallel}, N_u] = [20, 10]$ cases is $1.96/0.07 \sim 28$ which is close to $N_{ratio}^{3/2} = 9^{3/2} = 27$. Here, N_{ratio} is $N_{[60,30]}/N_{[20,10]} = 9$ when $N_{[60,30]}$ and $N_{[20,10]}$ are the total number of grid cells for $[N_{v_\parallel}, N_u] = [60, 30]$ case and the $[N_{v_\parallel}, N_u] = [20, 10]$ case, respectively. While $N_{ratio}^{3/2}$ is an expected scaling law for Eq. (83) [26], there have been several researches to improve the scaling. For instance, a fixed number of boundary points and interpolation are used in [27]. Also, an adaptive spline technique is introduced in [46] to achieve the desired accuracy under any circumstances. Although these methods are directly applicable to our model, the implementation is left as a future work. 'Source terms for δh and δg' is the time required to evaluate the right hand side of FEM equations, i.e., Eqs. (81) and (82). 'Solver for δh and δg' means the time to solve Eqs. (81) and (82). As mentioned in section 2.4, a direct LU factorization with the Intel MKL PARDISO library is used for the FEM solver. 'Field particle collision model' is the calculation of the conservation model for the linearized collision operator. The most time-consuming part is the calculation of 'Source terms for the weight evolution' which represents the calculation for the right hand side of Eq. (44). The computing cost of this part for linearized and nonlinear operators is about $60\% \sim 80\%$ higher than that of the Dougherty operator, since more computation is required to evaluate the coefficients α_i's for the linear and nonlinear models. 'Solver for the weight evolution' is the procedure of solving Eq. (44) once the source terms are evaluated. The total computing time of the nonlinear collision operator is about $70\% \sim 90\%$ higher than that of the Dougherty operator.

	Dougherty	Linearized	Nonlinear
Boundary conditions for δh and δg	0	0	0.07 (1.96)
Source terms for δh and δg	0	0	0.04 (0.44)
Solver for δh and δg	0	0	0.03 (0.37)
Field particle collision model	0	0.31 (2.59)	0
Source terms for the weight evolution	0.83 (7.52)	1.30 (11.51)	1.32 (13.53)
Solver for the weight evolution	0.14 (1.54)	0.13 (1.54)	0.15 (2.12)
Total	1.00 (9.8)	1.77 (15.8)	1.64 (18.6)

Table 3: Distribution of computing time for each collision model. Numbers without parentheses represents the $[N_{v_\parallel}, N_u] = [20, 10]$ case and numbers inside parentheses are results with $[N_{v_\parallel}, N_u] = [60, 30]$. The unit of time is normalized by the total computing time of the Dougherty collision model with $[N_{v_\parallel}, N_u] = [20, 10]$.

3.2 Relaxation of the bump-on-tail distribution

In this subsection, the benchmark test on the collisional relaxation of the bump-on-tail distribution is presented. More specifically, the initial condition $f(t=0)$ is given as follows.

$$f_{input} = \begin{cases} f_{M,U_\parallel=0} \times \frac{1}{2}\left[1+\cos(\frac{2\pi v_\parallel}{0.5 v_T})\right] & \text{if } v_\parallel \geq 0, \\ f_{M,U_\parallel=0} & \text{if } v_\parallel < 0, \end{cases} \tag{85}$$

where $f_{M,U_\parallel=0}$ is the Maxwellian distribution function with the zero mean drift velocity. The velocity domain for the test is $v_\parallel \in [-5v_T, 5v_T]$ and $u \in [0, 5v_T]$. The velocity grid size Δv is $0.25 v_T$ and the total simulation time is 10τ with the time step $\Delta t = 0.001\tau$.

The blue solid line in Fig. 4 represents the initially loaded $f_d(v_\parallel, u=0, t=0)$, while the red dashed line shows f_{input} of Eq. (85). Note that there are some regions with $f_d < 0$ due to the grid-scale gradient length of f_{input}, even though f_{input} itself is non-negative for the whole domain. When the nonlinear collision operator is applied, the distribution function is relaxed to the Maxwellian distribution function with the finite drift velocity and modified temperature, after a few collision times. The resulted $f_d(t = 10\tau)$ is represented as a solid black line in Fig. 4. Qualitatively similar results are obtained when we perform the same test with linearized and Dougherty operators.

To study the positivity-preserving property of each collision model, the maximum negative values of f_d in time are plotted in Fig. 5(a).

In the case of the Dougherty operator, the negative part of f_d is completely eliminated after $\sim$0.02 τ. For the linearized and nonlinear collision models, the negative value of f_d is significantly reduced within $\sim$0.1 τ and remains small for the rest of the simulation. In [32], the upwind flux is shown to be helpful in maintaining the low level of negativity induced by Dougherty collision operator. Although the absolute level of the negativity from the nonlinear collision operator is higher than the values from the Dougherty operator case, it seems that the upwind flux is still effective for controlling the negativity from the linearized and nonlinear collision operators. The evolution of entropy difference $\Delta S[\equiv S(t) - S(t=0)]$

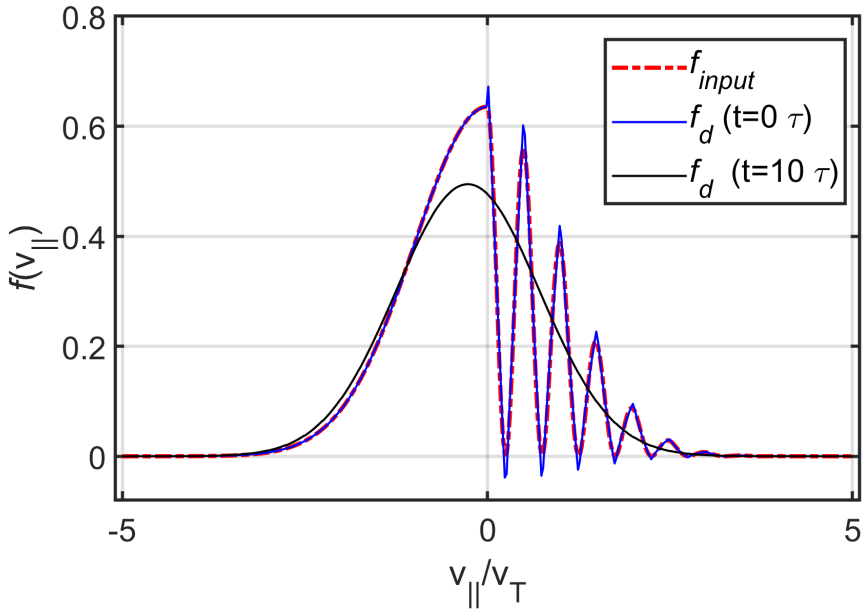

Figure 4: Relaxation of the bump-on-tail distribution function f with the nonlinear collision operator. All graphs are plotted at $u = 0$.

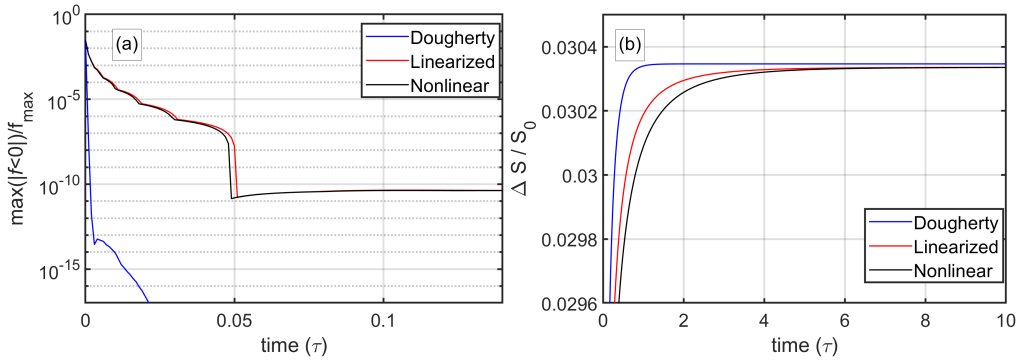

Figure 5: The evolution of (a) the maximum of negative f and (b) the normalized entropy difference ΔS. Here, S_0 is defined as $S(t = 0)$.

is also plotted in Fig.5(b). Here, the entropy S is defined as

$$S \equiv -\sum_{j,k} \int_{\Omega^{[j,k]}} d\vec{z} \mathscr{J} f_d^{[j,k]} \ln |f_d^{[j,k]}|. \tag{86}$$

The Dougherty operator shows the fastest time scale and the nonlinear operator exhibits the slowest time scale for the relaxation. Despite the different relaxation rate for each model, the entropy increases monotonically in time and converges to the same value for all cases, as expected.

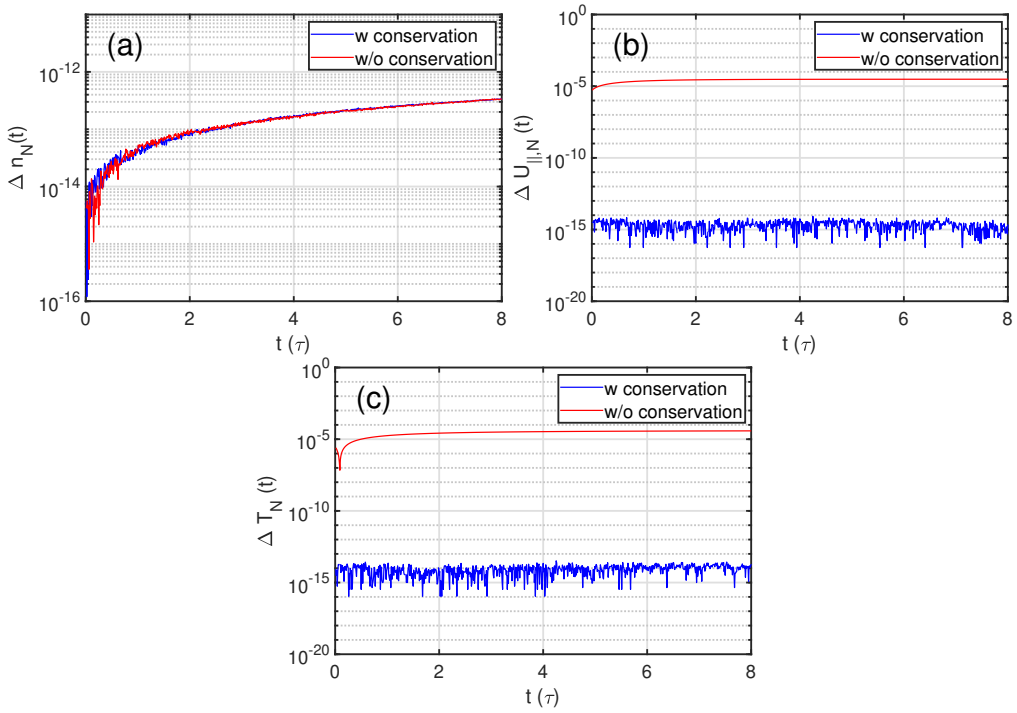

Figure 6: Time evolution of (a) the density n_N, (b) the parallel mean velocity $U_{\|,N}$, and (c) temperature T_N.

Fig. 6 shows time evolution of conserved quantities with the nonlinear collision operator. In Fig. 6, $\Delta n_N(t)$, $\Delta U_{\|,N}(t)$ and $\Delta T_N(t)$ are defined as

$$\Delta n_N(t) = \frac{M_0(t) - M_0(t=0)}{M_0(t=0)}, \tag{87}$$

$$\Delta U_{\|,N}(t) = \frac{M_1(t) - M_1(t=0)}{v_T M_0(t=0)}, \tag{88}$$

$$\Delta T_N(t) = \frac{M_2(t) - M_2(t=0)}{M_2(t=0)}, \tag{89}$$

where M_0, M_1 and M_2 are evaluated from Eqs. (45)-(47) with a time variable t. Here, n_N, $U_{\|,N}$ and T_N correspond to the density, the parallel mean velocity and the energy, respectively. For comparison, cases with and without the conservation operator L_A are plotted. Both cases show excellent density conservation since the collision operator is in the divergence form. Note that it is possible to improve the density conservation further, if one more free parameter $\beta_3 f$ is added to Eq. (58) and $\partial M_0/\partial t = 0$ is enforced. The numerical benefit of enforcing the density conservation directly, however, might not

be huge, since the level of the density error accumulation is tolerable in most simulation cases and the similar amount of density error is already generated through the collisionless part of the gyrokinetic equations. The momentum and energy from simulations without L_A increase gradually in time, while the case with L_A maintains the conservation properties. Without L_A, the rate of the temperature change, i.e., dT_N/dt, is about $2\times10^{-5}(/\tau)$.

3.3 Anisotropic temperature relaxation

For a given bi-Maxwellian probability distribution with $T_\perp \neq T_\parallel$, the temperatures of each direction are relaxed to the same value via the collisional process. Here, $T_\perp = \frac{m}{2n}\int v_\perp^2 f d\vec{v}$ and $T_\parallel = \frac{m}{n}\int v_\parallel^2 f d\vec{v}$ are temperatures perpendicular and parallel to the magnetic field, respectively. In Fig. 7, numerical results with Dougherty, linearlized and nonlinear collision models are compared with the following analytic formula [47].

$$\frac{dT_\perp}{dt} = -\frac{1}{2}\frac{dT_\parallel}{dt} = -\nu_T^\alpha\left(T_\perp - T_\parallel\right), \tag{90}$$

where

$$\begin{aligned}\nu_T^\alpha &= \frac{2\sqrt{\pi}n\ln\Lambda q^4}{\sqrt{m}T_\parallel^{1.5}}A^{-2}\left[-3+\frac{(A+3)\tan^{-1}A^{0.5}}{A^{0.5}}\right]\\ &= \frac{3}{2\sqrt{2}}\bar{\nu}\left(\frac{T}{T_\parallel}\right)^{1.5}A^{-2}\left[-3+\frac{(A+3)\tan^{-1}A^{0.5}}{A^{0.5}}\right].\end{aligned} \tag{91}$$

Here, the initial $T_\perp(t=0)$ is set as $1.3\times T_\parallel(t=0)$ and $A(t)$ is defined as $\frac{T_\perp(t)}{T_\parallel(t)}-1$. The velocity grid size is set as $0.5v_T$ and the time step size Δt is $0.001(\tau)$. Also, the velocity domains for the test are $v_\parallel \in [-5v_T, 5v_T]$ and $u \in [0, 5v_T]$. Although all of three operators show the relaxation process toward

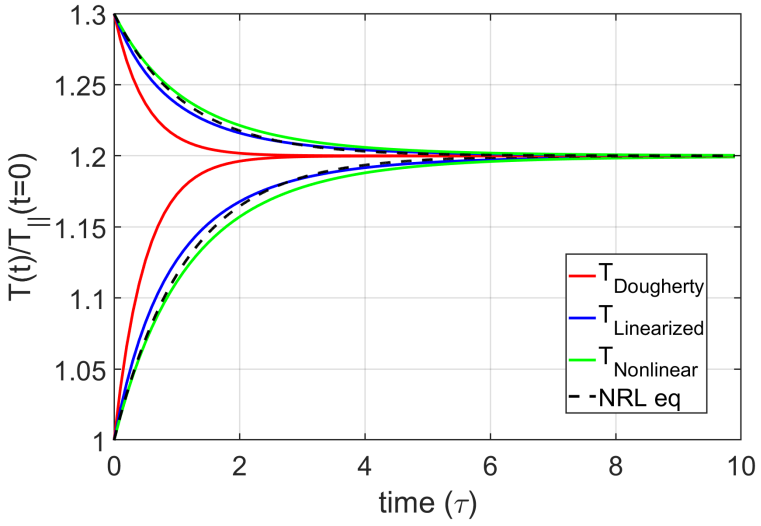

Figure 7: Temperature relaxation of each case with respect to the time.

$T_\parallel(t) = T_\perp(t) = 1.2T_\parallel(t=0)$, the relaxation rates are different for each collision operator. The relaxation rate of the nonlinear operator is slightly smaller than that of the linear operator [29], but closely follows

	Estimation from Eq. (92)	Dougherty	Linearized	Nonlinear
$\Delta t_{\max}/\tau$	5.0×10^{-3}	3.3×10^{-3}	4.2×10^{-3}	4.2×10^{-3}

Table 4: The maximum time step $\Delta t_{\max}$ from analytical estimation of Eq. (92) and anisotropic temperature relaxation simulations when $\Delta v_{\parallel} = \Delta u = 0.5 v_T$ and $\max(|v_{\parallel}|) = \max(u) = 5 v_T$.

the analytic formula over the simulation time. On the other hand, the relaxation rate of the Dougherty operator is about 2.5 times bigger than the analytic formula.

The numerical stability with different time step sizes is also tested for each collision operator. The maximum time step $\Delta t_{\max,theo}$ for the Dougherty collision operator with the SSP3 time integration can be estimated as [32]

$$\Delta t_{\max,theo}/\tau \sim \Delta_p \left[2C_{adv,p}(2p+1) \left\{ \frac{\max(|v_{\parallel}|)}{\Delta v_{\parallel}} + \frac{\max(u)}{\Delta u} \right\} + 4C_{dif,p} v_T^2 (p+1)^2 \left\{ \frac{1}{(\Delta v_{\parallel})^2} + \frac{1}{(\Delta u)^2} \right\} \right]^{-1}, \tag{92}$$

where $\Delta v_{\parallel}$ and Δu are the grid sizes in $v_{\parallel}$ and u directions. Also, Δ_p, $C_{adv,p}$ and $C_{dif,p}$ are functions of the basis order p. With $p = 2$ in this work, Δ_p, $C_{adv,p}$ and $C_{dif,p}$ are 2.512, 1.2 and 0.92, respectively. When $\Delta v_{\parallel} = \Delta u = 0.5 v_T$ and $\max(|v_{\parallel}|) = \max(u) = 5 v_T$, $\Delta t_{\max,theo}$ from Eq. (92) and $\Delta t_{\max}$ from simulations shown in Fig. 7 are given in Table 4. The level of agreement between the estimation and simulation results seems to be reasonable. Since SSP3 is an explicit method, numerical costs might be prohibitive at high collisionality regimes such as tokamak edge regions. Note that several implicit methods were developed for collision operators with the finite difference method [26] or the finite volume method [27], previously. Whether they can be directly applicable for DG collision operators will be tested as a future work.

IV Verifications of the implemented collision modules

In this section, we present neoclassical benchmark results for the various collision models introduced in the preceding sections. More specifically, numerical properties of each collision module are investigated for test cases of neoclassical heat diffusivity, poloidal flow, and Rosenbluth-Hinton residual potential with the collisional damping.

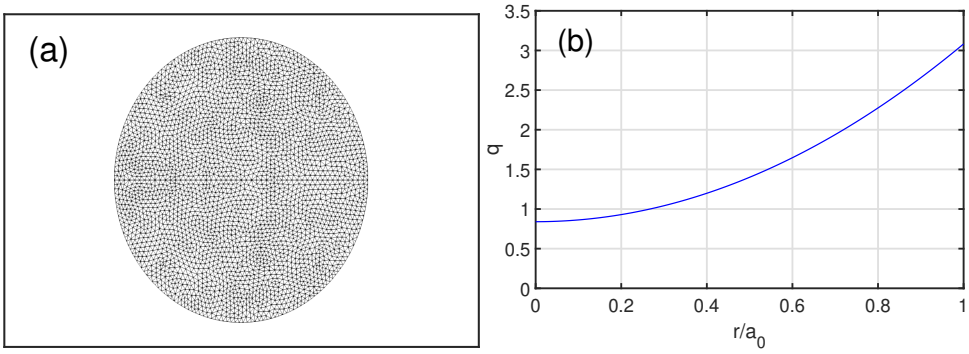

Figure 8: (a) A mesh in the configuration space and (b) the safety factor profile used for the verification.

All verification tests in the following subsections are carried out under the concentric circular magnetic geometry with a configuration space mesh of 5,846 vertices, as shown in Fig. 8(a). The number of cells used in velocity space is $N_{v_\parallel} = 30$ and $N_u = 10$. The velocity domains are $v_\parallel \in [-5v_T, 5v_T]$ and $u \in [0, 5v_T]$. Basic physics parameters commonly used in the following verifications are a major radius $R_0 = 1.7$m, a minor radius $a_0 = 0.6$m and magnetic field strength at the center $B_0 = 1.1$T. A concentric circular geometry without the Shafranov shift is used for the magnetic field geometry. The radial profile of the safety factor q is set as shown in Fig. $8(b)$ and only Deuteron-Deuteron collisions are considered for all test cases. Electrons are treated as fixed at a given initial state that electron profiles for density and temperature are same as corresponding initial ion profiles over an entire simulation. A set of gyrokinetic equations [38] without the FLR effect is used for the collisionless part of the simulation. Without the FLR effect, the equations of motion are effectively reduced to the drift kinetic model. Although these equations are not suitable for the quantitative micro-turbulence study, they are sufficient to investigate neoclassical physics in the drift kinetic limit. More details about the implementation of these equation for DG simulations are given in [35]. The third-order SSP3 Runge-Kutta method [41] is used for the time integration of gyrokinetic equations, as well as the collision operator. The normalized time step is defined as $dt = \frac{\Delta t}{R_0/v_T}$, where $\Delta t = \min\left(0.001\sqrt{2}\tau, 0.002R_0/v_T\right)$ and R_0/v_T is ion transit time. With this setup, parameter scans over normalized ion collision frequency, $\nu_* = \bar{\nu}/\left(\sqrt{2}\varepsilon^{3/2}v_T\nabla_\parallel\theta\right)$, is carried out by changing density, where $\varepsilon = r/R_0$ is inverse aspect ratio and $\nabla_\parallel\theta = 1/qR_0$ is used.

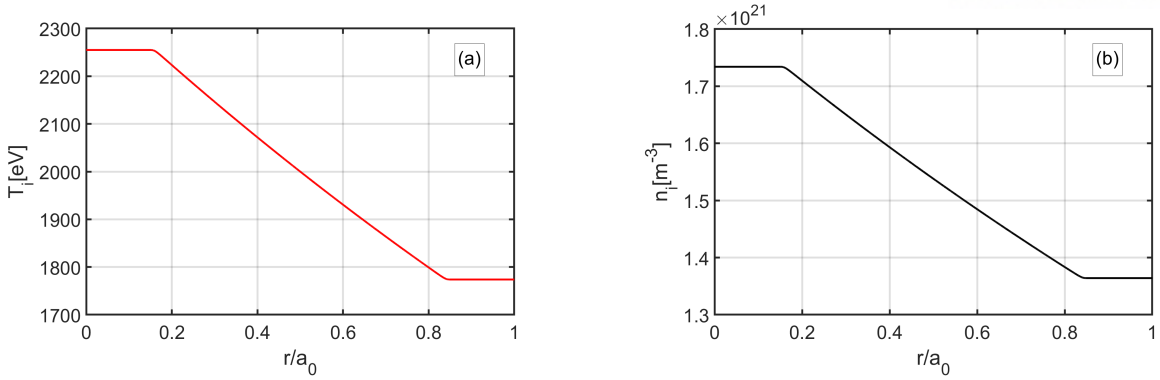

Figure 9: (a): Ion temperature profile. (b): Ion density profile at $\nu_* = 1.0$.

4.1 Neoclassical radial heat diffusivity

Chang and Hinton [48] predicted the ion thermal conductivity, L_i, for the arbitrary aspect ratio, plasma shaping and collision frequency as

$$L_i = n_i \varepsilon^{1/2} \frac{\rho_{i\theta}^2}{\sqrt{2}\tau} k_q, \tag{93}$$

where $\rho_{i\theta} = \frac{\sqrt{2} v_T m_i}{q_i B_\theta}$ is an ion poloidal gyroradius with the poloidal magnetic field B_θ, k_q is a dimensionless thermal conductivity coefficient [49]

$$k_q = \frac{0.66 + 1.88\varepsilon^{1/2} - 1.54\varepsilon}{1 + 1.03\nu_*^{1/2} + 0.31\nu_*} \left\langle B^2 \right\rangle \left\langle \frac{1}{B^2} \right\rangle + \frac{0.58\nu_*\varepsilon}{1 + 0.74\nu_*\varepsilon^{3/2}} \left(\left\langle B^2 \right\rangle \left\langle \frac{1}{B^2} \right\rangle - 1 \right), \tag{94}$$

and the angle bracket denotes flux surface averaging operation for a given parameter. In this thesis, we used thermal diffusivity χ_i for comparison by a relation $\chi_i = L_i / n_i$.

Parameter scans are conducted for normalized ion collision frequencies ν_*=0.05, 0.1, 0.5, 1, 5, and 10. Initial density and temperature profiles are monotonically decreasing linear functions with flat buffer regions around the radial boundaries. At center of the radial domain ($r/a_0 = 0.5$), density and temperature gradients are set to $R/L_{n_i} = 1$ and $R/L_{T_i} = 1$, respectively, where $L_{n_i} \equiv \left| \frac{1}{n_i} \frac{dn_i}{dr} \right|^{-1}$ and $L_{T_i} \equiv \left| \frac{1}{T_i} \frac{dT_i}{dr} \right|^{-1}$. Temperature at the radial center is fixed to $T_i = 2$keV while density changes according to a parameter of the normalized ion collision frequency. Fig. $9(a)$ and $9(b)$ show the temperature and density profiles at $\nu_* = 1.0$. Total simulation time is decided by a criterion $t_{tot} = \max\left(\sqrt{2}\tau, 20R_0/v_T\right)$.

Fig. 10 shows numerical heat diffusivities for each collision module of the test particle, linearized, nonlinear, and Dougherty collision operators against the Chang-Hinton analytic formula. The numerical values are obtained by moving average over 500 time steps of window in $(0.9t_{tot}, t_{tot})$, where background profile change is comparatively mild after its relaxation. We observe that all numerical results follow analytic trend that radial heat diffusivity increases as the collision frequency increases. In addition, all collision models except the Dougherty show reasonable agreement with the analytic formula. Particularly, the maximum difference between the analytic formula and the nonlinear collision result is about 20% at $\nu_* = 5.0$. Furthermore, we found that χ_is for the Dougherty operator are 2 or 3 times higher than χ_is of the other numerical operators, which would be because of enhanced collisionality for

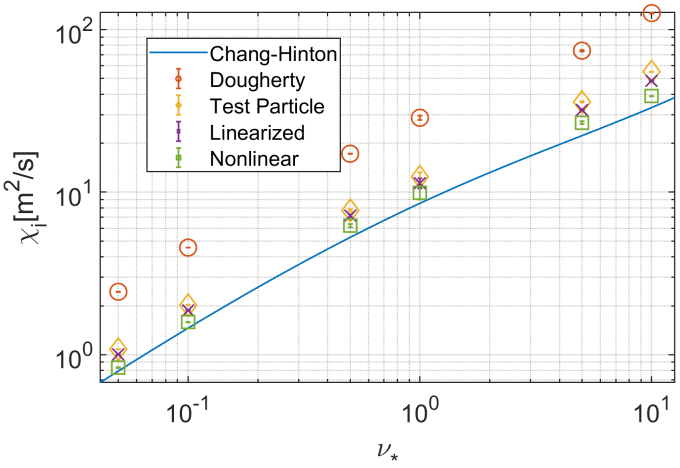

Figure 10: Comparison of the heat diffusivity at $\varepsilon = 0.1725$ among numerical collision results and theory. ◯(red): the Dougherty operator, △(yellow): the test particle operator, ×(purple): the linearized operator, □(Green): the nonlinear collision operator, and ——(a blue solid line) : the Chang-Hinton formula

the high energy ions in the Dougherty model. Lastly, the nonlinear operator exhibits slightly smaller heat diffusivity χ_i than the linear operator as observed in [50].

4.2 Neoclassical poloidal flow

To verify the developed collision operators against neoclassical poloidal flow theory, we conducted parameter scans over the same set of collisionality with the same simulation setup for the neoclassical heat diffusivity illustrated in the preceding subsection 4.1. In this poloidal flow test, a dimensionless flow coefficient $k_{\|}$ is inferred by poloidal velocity obtained in a simulation via relation as follows.

$$V_\theta = k_{\|} cIB_\theta \left(Ze\left\langle B^2\right\rangle\right)^{-1} dT_i/d\psi, \tag{95}$$

where $I = RB_\zeta$ and B_ζ is the toroidal magnetic field.

Fig. 11 shows the parallel flow coefficient $k_{\|}$ evaluated from numerical collision operators and the Sauter formula [51],

$$k_{\|} = -\left[\frac{1}{1+0.5\sqrt{\nu_*}}\left(\frac{-1.17 f_c}{1-0.22 f_t - 0.19 f_t^2} + 0.25\left(1-f_t^2\right)\sqrt{\nu_*}\right) + 0.315\nu_*^2 f_t^6\right]\frac{1}{1+0.15\nu_*^2 f_t^6}, \tag{96}$$

where $f_t = 1 - f_c$ is trapped fraction of particles. The values of the numerical results in the figure are obtained using the moving average as done in the subsection 4.1. All numerical collision operators clearly exhibit sign flip of the coefficient $k_{\|}$ in increasing collision frequency as predicted by the theory. Also it is noticeable that the $k_{\|}$ for the Dougherty operator is negatively shifted over most frequency domain and consequently transition of the sign flip occurs at smaller frequency than the others.

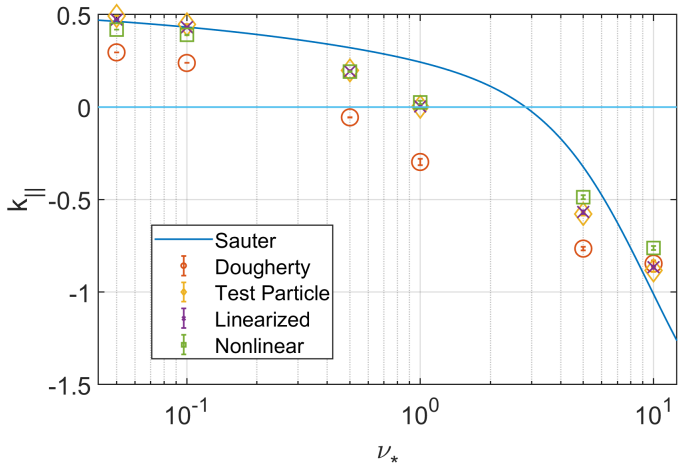

Figure 11: Comparison of the parallel flow coefficient at $\varepsilon = 0.1725$ among numerical collision results and theory. ◯(red): the Dougherty operator, △(yellow): the test particle operator, ×(purple): the linearized operator, □(Green): the nonlinear collision operator, and —(a blue solid line) : the Sauter formula.

	$\nu_* = 0.1$		$\nu_* = 1.0$	
	γ	b	γ	b
Dougherty	0.032	0.014	0.12	0.012
Test Particle	0.026	0.017	0.10	0.013
Linearized	0.026	0.016	0.10	0.012
Nonlinear	0.025	0.017	0.096	0.012
Xiao (YX) et al.	0.023	0.016	0.22	0.016

Table 5: Exponential fitting of residual potential behavior

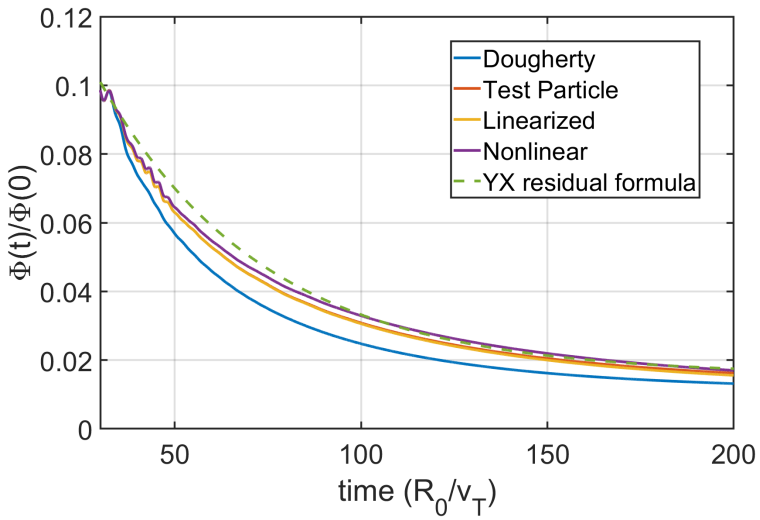

Figure 12: Damping of residual potential at $\nu_* = 0.1$.

4.3 Damping of residual potential

In this subsection, the benchmark results for the collisional damping of zonal flow are presented. Since the zonal flow can have crucial impacts on regulating the turbulent heat flux, the collisional damping of zonal flow is an important issue. In the collisional case, initially loaded potential perturbations will be damped to the certain residual value B_p^2/B^2 [52] which is different from the residual value of the collisionless case. For the benchmark, we compare the simulation results with the analytic formula of Xiao et al. [53] as follows.

$$\phi_k/\phi_k(t=0) = \frac{\varepsilon^2/q^2}{1+\varepsilon^2/q^2} \times \left[1 + \frac{1-\Theta}{\Theta+\varepsilon^2/q^2} \exp\left\{-\frac{3\sqrt{\pi}\left(1+\varepsilon^2/q^2\right)\gamma\bar{\nu}t}{4\left(\Theta+\varepsilon^2/q^2\right)}\right\}\right] \tag{97}$$

where $\Theta = 1.635\varepsilon^{3/2} + \varepsilon^2/2 + 0.360\varepsilon^{5/2}$ and $\gamma = 0.4\left(1.46\sqrt{\varepsilon} + 1.32\varepsilon\right)$.

To investigate the collisional effect on the zonal flow, a sinusoidal radial electric field with $k_r\rho_i \sim 0.12$ is applied as an initial condition. Here, $\rho_i = \frac{v_T m_i}{q_i B}$ is the ion gyroradius and the ratio of the initial ExB flow velocity to the v_T is 0.015. Also, flat density and temperature profiles are used as initial inputs. To separate initial GAM oscillations from the collisional damping, the collision modules are turned on at $t = t_{init} \equiv 30(R_0/v_T)$ when the E_r reaches the steady state after the collisionless neoclassical damping. Two cases with ν_* = 0.1 and 1.0 are tested and we compare $\Phi(t) = E_r(t) - \nabla p(t)/ne$, instead of $\phi(t)$, with the analytic formulas to exclude contributions from the pressure gradients and the boundary effects.

Fig. 12 shows long time behavior of $\Phi(t)$ with $\nu_* = 0.1$. All results from different collision models do not deviate much during the relaxation phase and converge asymptotically - In the figure, a line from the test particle model is mostly overlaid by the line from the linearized model. Maximum difference of the residual ratio over 200 transit time is 9.34% for $\nu_* = 0.1$ and 9.14% for $\nu_* = 1.0$ between Dougherty and the nonlinear operator. For easier comparison, we fit the data with $y(t) = [\Phi(t_{init})/\Phi(0) - b]\exp[-\gamma(t - t_{init})] + b$, where γ is the damping rate and b is the residual value after long term simulation. The results from the fitting are summarized in table 2. From the data, we can see that all b values from the simulation and Xiao closely agree within $\sim$ 4 % relative error range of the potential at $t = t_{init}$. Note that this residual value is closely related to the energy conservation between electric field and toroidal angular momentum, as well as the radial force balance. In addition, we found that the collisional damping rate γ from the Dougherty operator is about 20 percent higher than the values from the other numerical models. This is consistent with the results of previous sections in which the Dougherty model exhibits the enhanced collisionality. Also, we observe that the numerical γ does not linearly increase with the collision frequency while that from the analytic formula in Eq. (97) does.

4.4 Collisional effects on GAM frequency and damping rates

Previously, collisional effects on GAM were studied with fluid models and kinetic models [54]. From those studies, it has been known that the real frequency of GAM (ω_{GAM}) decreases to the frequency of the fluid limit as the collisionality increases, since collisions weaken the pressure anisotropy. On the

other hand, the damping rate of GAM (γ_{GAM}) increases with the increasing collisionality at the low collisionality regime, while γ_{GAM} decreases back to the collisionless level at the high collisionality regime. To verify that those behaviors can be reproduced with the collision model of this work, benchmark results of the collisional GAM damping are presented in this subsection. For the benchmark, we compare the simulation results to the following theoretical formula based on the number and energy conserving Krook operator [55].

$$\omega_{GAM} = \frac{v_T}{R_0}\sqrt{2}\left[\frac{7}{4}+\tau_e-\frac{(3\pi/32)\,{\nu_N}^2}{7+4\tau_e+(9\pi/8)\,{\nu_N}^2}\right]^{1/2}, \tag{98}$$

$$\gamma_{GAM} = \frac{v_T}{R_0}\frac{\left(\sqrt{\pi}/4\right)\nu_N}{14+8\tau_e+(9\pi/4)\,{\nu_N}^2}, \tag{99}$$

where τ_e is the ratio between the electron temperature and the ion temperature. ν_N is a normalized collisionality and defined as $\bar{\nu}R_0/v_T$. Since the adiabatic electron model is used in this work, we only present the results with $\tau_e = 0$, i.e. no kinetic electron effect. The $k_r\rho_i$ of the initial perturbation is 0.12. Note that there is no safety factor dependence in Eqs. (98) and (99), since they are derived in the infinite q limit. Also, several collisionless mechanisms such as the Landau damping and finite orbit effects [56] are missed as well. Fig. 13 shows ω_{GAM} from simulations and analytic formulas with varying ν_N. Since it is impractical to perform a simulation with an infinite q, several simulations with different safety factors are performed to examine the change of ω as the q increases. As shown in Fig. 13, ω_{GAM} tends to decrease as q increases. For collisionless cases, the following formulas of ω_{GAM} and γ_{GAM} with varying q were derived in [57, 58].

$$\omega_{GAM} = \frac{v_T}{R_0}\sqrt{\frac{7}{2}}\sqrt{1+\frac{46}{49q^2}}, \tag{100}$$

$$\begin{aligned}\gamma_{GAM} = \frac{v_T}{R_0}q\sqrt{\frac{\pi}{2}}\left[1+\frac{46}{49q^2}\right]^{-1}&\left[\exp(-\hat{\omega}_G^2)\left\{\hat{\omega}_G^4+\hat{\omega}_G^2\right\}\right.\\ &\left.+\frac{1}{32}\left(\sqrt{2}qk_r\rho_i\right)^2\exp(-\hat{\omega}_G^2/4)\left\{\frac{\hat{\omega}_G^6}{16}+\frac{\hat{\omega}_G^4}{2}+3\hat{\omega}_G^2\right\}\right],\end{aligned} \tag{101}$$

where $\hat{\omega}_G$ is defined as $qR_0\omega_{GAM}/(\sqrt{2}v_T)$. Analytic values of ω_{GAM} from Eq. (100) are plotted in Fig. 13 as filled symbols and show good agreements with simulations results. Therefore the decrease of ω_{GAM} with increasing q can be explained by the collisionless part of the simulations. As shown in Fig. 13, ω_{GAM} decreases with increasing ν_N, as predicted by the analytic formula Eq. (98). Also, ω_{GAM} approaches to the analytic formula as q increases, which is consistent to the fact that the analytic formula is based on the infinite q assumption.

The total γ_{GAM} which is affected by both of collisionless and collisional damping mechanism is shown in Fig. 14(a). Analytic predictions from Eq. (101) for $\nu_N = 0$ are also plotted in Fig. 14(a) as filled symbols. Theoretically, γ_{GAM} tends to decrease, although not monotonically, with increasing q since the number of resonant particles becomes smaller with higher q. [56, 59] γ_{GAM} values from simulations with $\nu_N = 0$ are qualitatively consistent to the theoretical prediction, although the level of agreement with the analytical prediction Eq. (101) is less satisfactory than ω_{GAM} cases shown in Fig. 13. At the low collisionality, γ_{GAM} increases as ν_N increases, while it decreases with increasing ν_N at the high collisionality. This

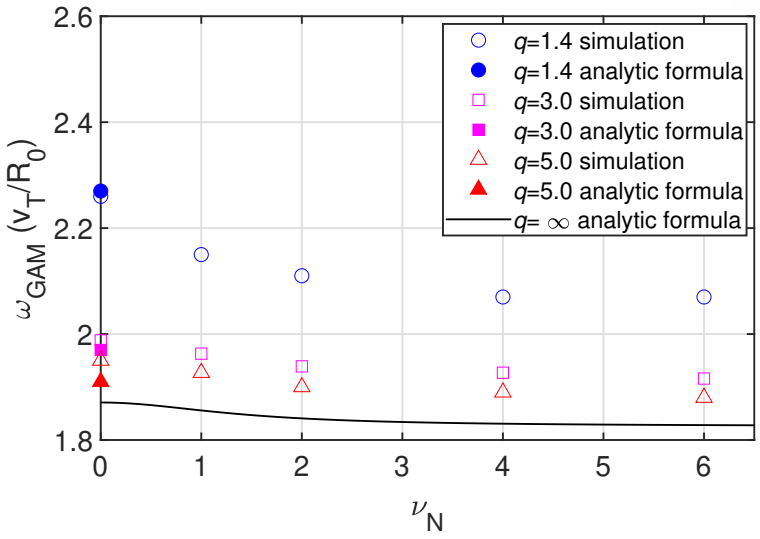

Figure 13: Comparison of the real frequency (ω_{GAM}) of GAM from simulations with the nonlinear collision operator and the analytic formula. ν_N is defined as $\bar{\nu}R_0/v_T$. ◯(blue): q = 1.4, □(magenta): q = 3.0, △(red): q = 5.0, and ——(a black solid line) : the analytic formula, Eq. (98) [55]. Filled symbols represent values from the analytic formula Eq. (100) for $\nu_N = 0$ cases [57,58].

result agrees with the theoretical prediction qualitatively. To focus more on the collisional effects on γ_{GAM}, the change of damping rate $\Delta\gamma_{GAM}$ defined as $\gamma(\nu_N) - \gamma(\nu_N = 0)$ is plotted in Fig. 14(b). Like the case of ω_{GAM}, $\Delta\gamma_{GAM}$ approaches to the analytic formula as q increases. As a partial summary of this subsection, the collisional effects on GAM from the simulations with the newly developed collision module are consistent to the theoretical prediction, although the quantitative verification is not available.

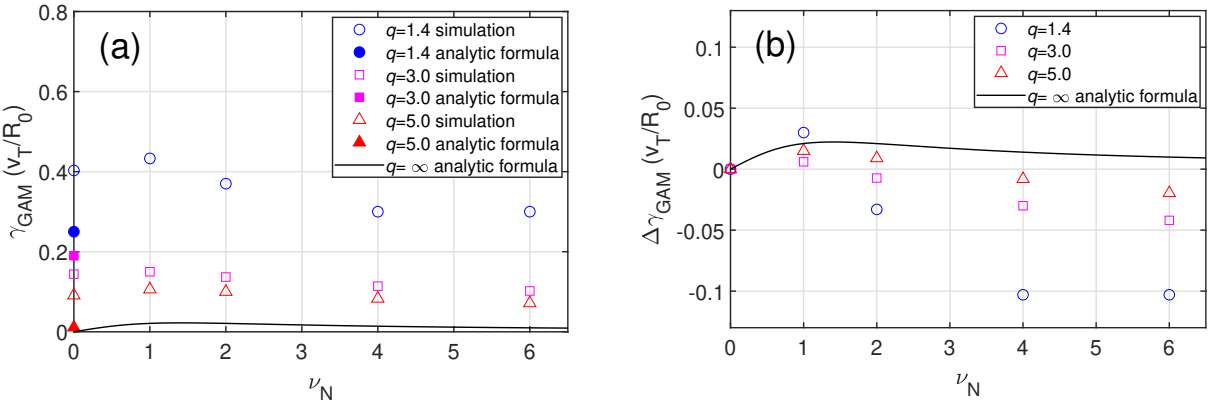

Figure 14: (a) the total damping rate (γ_{GAM}) of GAM as a function of the normalized collisionality ν_N and (b) the change of damping rate $\Delta\gamma = \gamma(\nu_N) - \gamma(\nu_N = 0)$. ν_N is defined as $\bar{\nu}R_0/v_T$. ◯(blue): q = 1.4, □(magenta): q = 3.0, △(red): q = 5.0, and ——(a black solid line) : the analytic formula, Eq. (99) [55]. Filled symbols represent values from the analytic formula Eq. (101) for $\nu_N = 0$ cases [57,58].

V Conclusion

A nonlinear collision operator is formulated and implemented for the gyrokinetic simulations with the discontinuous Galerkin (DG) scheme. For better numerical efficiency, the Rosenbluth-MacDonald-Judd (RMJ) form is implemented instead of the Landau integral form. In addition to the nonlinear collision operator, linearized and Dougherty collision models are also implemented to assess the benefits and drawbacks of each model. In this work, we only consider the self-collisions of a single ionic species.

Conservation properties of collision models are important for the stability and reliability of the long time gyrokinetic simulations. Due to the divergence structure of the formulation, the density conservation is guaranteed numerically. For the conservation of the parallel momentum and energy, a simple advection-diffusion model, i.e., L_A, with two free parameters is adopted for the Dougherty and nonlinear collision operators. By using L_A, the conservation of the momentum and energy is enforced up to the machine accuracy. In the case of the linear collision operator, the linearized field particle collision operator is adopted as another way to enforce the conservations.

While the DG method is used to describe the particle distribution function f, the finite element method (FEM) with the cubic B-spline basis is applied to evaluate the Rosenbluth potentials h and g, since the 2nd order derivatives of h and g are required for the nonlinear collision operator. Especially, the analytic solutions for the equilibrium parts of h and g are utilized to improve the numerical resolution for the case where f is close to the Maxwellian distribution function f_M.

Several benchmark problems are solved to test the numerical properties of the developed collision models. The residuals of $C(f_M)$, i.e., $L_2^{\Delta v}$, are evaluated for each collision model with the initial condition of $f = f_M$. All models show similar convergence rates of $L_2^{\Delta v} \propto (\Delta v)^{1.6}$ with varying grid sizes Δv. While linearized and nonlinear operators exhibit the same level of $L_2^{\Delta v}$, $L_2^{\Delta v}$ from the Dougherty operator is smaller than those from the other operators. $L_2^{\Delta v}$ of the linearized operator without cross-diffusion terms ($\propto \partial^2/\partial v_\parallel \partial u$) is close to that of the Dougherty operator, which indicates that $L_2^{\Delta v}$ of the current model is sensitive to the cross-diffusion in the velocity space. In terms of the numerical cost for each model, the computing times for the linear and nonlinear operators are about $70\% \sim 90\%$ higher than the time required for the Dougherty operator for the range of parameters tested in this work.

As another benchmark problem, the collisional relaxation of f from the bump-on-tail distribution to f_M is tested. From the test, the numerical stability with the locally negative f, the monotonically increasing entropy in time and the conservation properties are verified for the developed nonlinear collision model. In the anisotropic temperature relaxation test with $T_\perp \neq T_\parallel$ as an initial condition, the results from the linear and nonlinear models agree well with the analytic prediction, while the Dougherty operator tends to overestimate the relaxation rate by ~ 2.5 times.

To analyze characteristics of each collision model in tokamak magnetic geometry, a few neoclassical benchmark tests are performed. The neoclassical heat flux and poloidal flow from linear and nonlinear collision models show a good agreement with theoretical values. On the other hand, the heat flux from the Dougherty operator is about 2 or 3 times bigger than results from the other operators, which can be explained by the neglected velocity dependency in the Dougherty operator. The collisional damping of

zonal flow is also tested with initial electric field perturbations. For $\nu_* = 0.1$, the damping rates from linear and nonlinear collision models are $\sim 15\%$ bigger than the analytic formula. On the other hand, the damping rates from simulations for $\nu_* = 1.0$ are about 50 % of the theoretical prediction. In both cases, the damping rates from the Dougherty model are $\sim 20\%$ higher than those from other collision models. In terms of residual E_r after the collisional damping, all collision models show similar results close to the theoretical values. In addition, the collisional effect on the GAM frequency and damping rate is tested. From the test, it is shown that the simulation results agree with the analytic formula qualitatively in the relevant limit.

Since the multi-species collision is not included in this work, a natural direction for further research would be the implementation of inter-species collision operators. Contrary to the self-collision, the velocity domains of different species can be significantly disparate from each other if the mass ratio between species is not of order unity. In this case, additional numerical operations might be required to interpolate the Rosenbluth potentials from one velocity space to another. We can leverage work by Taitano et al. [60] that introduces multipole expansion with adaptive mesh to treat the different scales. Also, the conservation of momentum and energy for inter-species collisions is not a trivial problem. These issues related to multi-species collisions with the DG scheme will be reported separately in near future.

Most test cases in this work show similar numerical behavior among the linear and nonlinear collision models. This is partially because the distribution function stays near f_M in closed magnetic field line system used in those tests. On the other hand, the distribution can deviate significantly from f_M with open field lines, since ions suffer the ion orbit loss and the electrons stream into the machine wall along the field lines. Therefore, more noticeable differences between linear and nonlinear models are expected at the tokamak edge region where the closed and open field lines are present together. Quantitative analysis on the nonlinear collisional effect at the edge region is left as a future work.

A Relations between introduced collision operators

The linearized collision operator, the test particle collision operator, and the Dougherty operator can be derived in order from the Fokker-Planck collision operator. Rosenbluth, MacDonald, and Judd introduced a potential theory to Fokker-Planck-Landau equation [2],

$$\left(\frac{\partial f_a}{\partial t}\right)_c = \sum_b -\Gamma_{ab}\left[\frac{m_a+m_b}{m_b}\frac{\partial}{\partial \boldsymbol{v}}\cdot\left(f_a\frac{\partial h_b}{\partial \boldsymbol{v}}\right) - \frac{\partial^2}{\partial \boldsymbol{v}\partial \boldsymbol{v}} : \left(f_a\frac{\partial^2 g_b}{\partial \boldsymbol{v}\partial \boldsymbol{v}}\right)\right] \tag{A.1}$$

$$= \sum_b -\Gamma_{ab}\left[\frac{m_a}{m_b}\frac{\partial}{\partial \boldsymbol{v}}\cdot\left(f_a\frac{\partial h_b}{\partial \boldsymbol{v}}\right) - \frac{\partial}{\partial \boldsymbol{v}}\cdot\left\{\frac{\partial f_a}{\partial \boldsymbol{v}}\cdot\left(\frac{\partial^2 g_b}{\partial \boldsymbol{v}\partial \boldsymbol{v}}\right)\right\}\right], \tag{A.2}$$

$$\equiv \sum_b C_{ab}(f_a, f_b)$$

$$\nabla_v^2 h_b = -f_b, \tag{A.3}$$

$$\nabla_v^2 g_b = h_b, \tag{A.4}$$

where the coefficient Γ_{ab} is $\{4\pi q_a q_b/m_a\}^2 \ln\Lambda_{ab}$ in CGS (or $\{q_a q_b/(m_a\varepsilon_0)\}^2 \ln\Lambda_{ab}$ in MKS [3, 47, 61] with the vacuum permittivity ε_0), and $\ln\Lambda_{ab}$ is the Coulomb logarithm for an incident species a and a target species b. q_s and m_s are charge and mass for species s, respectively. In this appendix, $\boldsymbol{v}$ represents the original velocity coordinate which is not transformed into gyrokinetic variables. Here, Rosenbluth potentials are defined as

$$h_b = \frac{1}{4\pi}\int d\boldsymbol{v}' f_b(\boldsymbol{v}')\left|\boldsymbol{v}-\boldsymbol{v}'\right|^{-1}, \tag{A.5}$$

$$g_b = \frac{1}{8\pi}\int d\boldsymbol{v}' f_b(\boldsymbol{v}')\left|\boldsymbol{v}-\boldsymbol{v}'\right|. \tag{A.6}$$

Splitting the probability distribution function f into equilibrium part f_0 and perturbed part δf as $f = f_0 + \delta f$, the collision operator can be decomposed based on its bilinearity as

$$C_{ab}(f_a, f_b) = C_{ab}(f_{a0}, f_{b0}) + C_{ab}(\delta f_a, f_{b0}) + C_{ab}(f_{a0}, \delta f_b) + C_{ab}(\delta f_a, \delta f_b). \tag{A.7}$$

The first term is contribution from two equilibrium distribution, which vanishes when f_{a0} and f_{b0} are Maxwellian distribution functions with same mean velocity and temperature. The second and third terms are called a test particle collision operator and a field particle collision operator, respectively. The last term is a nonlinear part, which is usually neglected on the assumption of $\delta f \ll f_0$ in linearization process. Considering the validity regime of the approximation, the assumption would limit the region of simulation domain in Tokamaks and consequently hinder a whole device modeling.

By introducing Maxwellian distribution function f_M as an equilibrium distribution function, $f_0 = f_M$ into Eqs. (A.3) and (A.4), we can make further progress with the Rosenbluth potentials to be analytically expressed in the first and second terms of Eq. (A.7). The resulting test particle collision operator

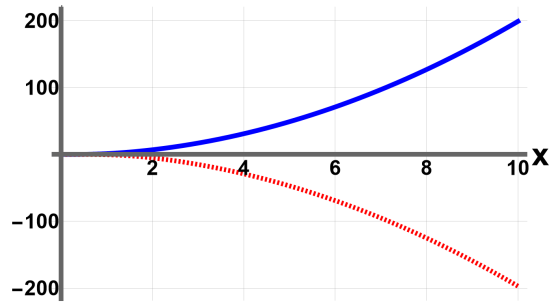

(a) $F_1(x)$(the blue solid line) and $3F_2(x)$(the red dashed line)

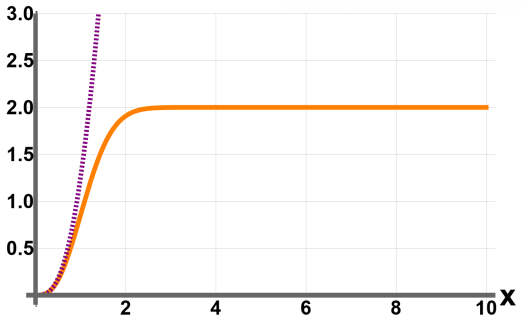

(b) $F_1(x)+3F_2(x)$(the orange solid line) and $F_1(x)$(the purple dashed line)

Figure A.1: Global behavior of $F_1(x)$, $3F_3(x)$ and their sum

including the equilibrium part contribution becomes [61]

$$C_{ab}(f_a, f_{b,M}) = -\frac{\Gamma_{ab}}{8\pi} n_b \nabla \cdot \left[\frac{m_a}{m_b} \boldsymbol{R}_{ab,M} f_a - \boldsymbol{D}_{ab,M} \cdot \nabla f_a \right], \tag{A.8}$$

$$\boldsymbol{R}_{ab,M} = -\frac{\boldsymbol{v}'}{v'^3} \left[F_1(x) + 3F_2(x) \right], \tag{A.9}$$

$$\boldsymbol{D}_{ab,M} = \frac{v_{T_b}^2}{v'^3} \left[\boldsymbol{I} F_1(x) + 3 \frac{\boldsymbol{v}'\boldsymbol{v}'}{v'^2} F_2(x) \right], \tag{A.10}$$

$$F_1(x) = x \frac{d\mathrm{erf}(x)}{dx} + (2x^2 - 1)\mathrm{erf}(x), \tag{A.11}$$

$$F_2(x) = \left(1 - \frac{2}{3}x^2 \right) \mathrm{erf}(x) - x \frac{d\mathrm{erf}(x)}{dx}, \tag{A.12}$$

where $x = \frac{v'}{\sqrt{2} v_{T_b}}$, $v_{T_b} \equiv \sqrt{\frac{T_b}{m_b}}$, and $\boldsymbol{v}' = \boldsymbol{v} - \boldsymbol{U}_b$. Here, n_s, $\boldsymbol{U}_s$ and T_s are the density, mean fluid velocity and temperature for the species s, respectively. Also, $\mathrm{erf}(x) = \frac{2}{\sqrt{\pi}} \int_0^x e^{-t^2} dt$ is the error function. The Rosenbluth potentials in this context [45] correspond to

$$h_{b,M} = \frac{n_b}{4\pi} \frac{1}{\sqrt{2} v_{T_b}} \frac{\mathrm{erf}(x)}{x}, \tag{A.13}$$

$$g_{b,M} = \frac{n_b}{8\pi} \frac{v_{T_b}}{\sqrt{2}} \frac{1}{x} \left[x \frac{d\mathrm{erf}(x)}{dx} + (1 + 2x^2)\mathrm{erf}(x) \right]. \tag{A.14}$$

These expressions for the Rosenbluth potentials contain additional factors in front to Hazeltine and Waelbroeck [61] with correcting typos - See the factors in Eqs. (A.5) and (A.6).

By taking a small speed limit $x \to 0$, we can analytically proceed further with Eq. (A.8) using asymptotic expansion of the error function, $\mathrm{erf}(x) = \frac{2}{\sqrt{\pi}} \left(x - \frac{x^3}{3} \right) + O(x^5)$. The factor $F_1(x)$ and $F_2(x)$ are reduced to

$$F_1(x) = \frac{8}{3\sqrt{\pi}} x^3 \left(1 - \frac{1}{5}x^2 \right) + O(x^7) \quad \text{as } x \to 0, \tag{A.15}$$

$$F_2(x) = -\frac{16}{45\sqrt{\pi}} x^5 \left(1 - \frac{3}{7}x^2 \right) + O(x^9) \quad \text{as } x \to 0, \tag{A.16}$$

respectively. This indicates that the contribution from the cross diffusion terms in the small speed limit is $O(x^2)$ smaller than that of the diagonal diffusion terms in Eq. (A.10). Correspondingly, an asymptotic

value of the dragging factor in the bracket of Eq. (A.9) leads to

$$F_1(x)+3F_2(x)=\frac{8}{3\sqrt{\pi}}x^3\left(1-\frac{3}{5}x^2\right)+O(x^7)\sim\frac{8}{3\sqrt{\pi}}x^3 \quad \text{as } x\to 0. \tag{A.17}$$

As a side note, the other asymptotic limit as $x\to\infty$ yields $F_1(x)+3F_2(x)\sim 2$ that results in the dragging coefficient approaches to $2/v^3$. Note that this factor is also related to $D_{ab,M}$ tensor in v-direction through a following relation,

$$\boldsymbol{v}'\cdot\boldsymbol{D}_{ab,M}=\boldsymbol{D}_{ab,M}\cdot\boldsymbol{v}'=v_{Tb}^2\frac{\boldsymbol{v}'}{v'^3}\left[F_1(x)+3F_2(x)\right]=-v_{T_b}^2\boldsymbol{R}_{ab,M} \tag{A.18}$$

that results in Maxwellian at equilibrium. Fig. A.1 shows global behavior of the functions $F_1(x)$, $3F_2(x)$, and their sum. Even though $F_2(x)$ is $O(x^2)$ smaller than $F_1(x)$ in the small speed limit, it is appreciable around $x\sim 1$ and comparable with $F_1(x)$ in the high tail.

Asymptotic expressions for dragging and diffusion coefficients in the small speed limit are

$$\boldsymbol{R}_{ab,M}\sim-\frac{\boldsymbol{v}'}{v'^3}\frac{8}{3\sqrt{\pi}}\frac{v'^3}{2^{3/2}v_{T_b}^3}=-\frac{4}{3\sqrt{2\pi}}\frac{1}{v_{T_b}^3}\boldsymbol{v}', \tag{A.19}$$

$$\hat{\boldsymbol{v}}'\hat{\boldsymbol{v}}':\boldsymbol{D}_{ab,M}\sim\frac{v_{T_b}^2}{v'^3}\frac{8}{3\sqrt{\pi}}\frac{v'^3}{2^{3/2}v_{T_b}^3}=\frac{4}{3\sqrt{2\pi}}\frac{1}{v_{T_b}}=\frac{4}{3\sqrt{2\pi}}\frac{1}{v_{T_b}^3}v_{T_b}^2 \tag{A.20}$$

which agree with coefficients in the prototype of the Dougherty operator for the self-collision [6, 32],

$$C(f)=\nu\frac{\partial}{\partial\boldsymbol{v}}\cdot\left\{(\boldsymbol{v}-\boldsymbol{U})f+v_T^2\frac{\partial f}{\partial\boldsymbol{v}}\right\}. \tag{A.21}$$

Through this reduction process, we show that Dougherty operator neglects cross-diffusion $(\boldsymbol{I}-\hat{\boldsymbol{v}}'\hat{\boldsymbol{v}}'):\boldsymbol{D}_{ab,M}$. Terms in the curly bracket of Eq. (A.21) are designed to have (shifted) Maxwellian at equilibrium through diagonal drag-diffusion processes.

Although the well-known result $\nu\propto v_T^{-3}\propto T^{-3/2}$ is recovered, the slow speed approximation delimits the validity regime of the Dougherty operator to $v/v_T\ll 1$. Dougherty pointed out that constant drag coefficients cannot reflect the reduced collisionality for fast-moving particles [6, 9]. In other words, fast ions in high tails cannot be correctly treated. The extent of discrepancy due to the approximation can be observed in Figure. A.2. About 50% of the collision factor deviates near two times thermal speed $\sim 2v_T$ and the difference is getting significantly larger in higher speed of tails.

Under the strong magnetic field assumption, the cylindrical coordinates $(v_\parallel, v_\perp)$ with a symmetry in the gyroangle v_θ is a natural choice, where $v_\parallel$ and $v_\perp$ are velocity components parallel and perpendicular

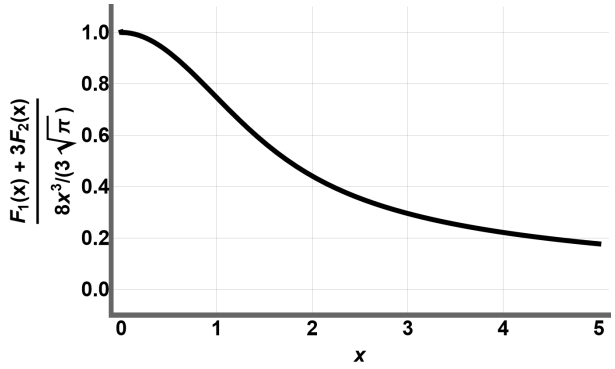

Figure A.2: Ratio of exact to asymptotic values as $x \to 0$ (i.e., $v \to 0$) for $F_1(x) + 3F_2(x)$, described in Eq. (A.17)

to local magnetic field, respectively. Eq. (A.8) in the cylindrical coordinate can be explicitly written as

$$\begin{aligned}
C_{ab}(f_a) &= C(f_a, f_{b,M}) \\
&= n_b \frac{\Gamma_{ab}}{8\pi} \left[\frac{\partial}{\partial v_\parallel} \frac{1}{v'^3} \left\{ \frac{m_a}{m_b}(F_1 + 3F_2) v'_\parallel f_a + \left(F_1 + 3F_2 \frac{v'^2_\parallel}{v'^2} \right) v^2_{T_b} \frac{\partial f_a}{\partial v_\parallel} + 3F_2 v^2_{T_b} \frac{v'_\parallel v_\perp}{v'^2} \frac{\partial f_a}{\partial v_\perp} \right\} \right. \\
&\quad \left. + \frac{1}{v_\perp} \frac{\partial}{\partial v_\perp} \frac{v_\perp}{v'^3} \left\{ \frac{m_a}{m_b}(F_1 + 3F_2) v_\perp f_a + \left(F_1 + 3F_2 \frac{v^2_\perp}{v'^2} \right) v^2_{T_b} \frac{\partial f_a}{\partial v_\perp} + 3F_2 v^2_{T_b} \frac{v_\perp v'_\parallel}{v'^2} \frac{\partial f_a}{\partial v_\parallel} \right\} \right] \\
&= \bar{\nu}_{ab} \frac{3\sqrt{\pi}}{8} \left[\frac{\partial}{\partial v_\parallel} \frac{1}{x^3} \left\{ \frac{m_a}{m_b}(F_1 + 3F_2) v'_\parallel f_a + v^2_{T_b} \left(F_1 + \frac{3v'^2_\parallel F_2}{2v^2_{T_b} x^2} \right) \frac{\partial f_a}{\partial v_\parallel} + \frac{3F_2}{2x^2} v_\perp v'_\parallel \frac{\partial f_a}{\partial v_\perp} \right\} \right. \\
&\quad \left. + \frac{1}{v_\perp} \frac{\partial}{\partial v_\perp} \frac{v_\perp}{x^3} \left\{ \frac{m_a}{m_b}(F_1 + 3F_2) v_\perp f_a + v^2_{T_b} \left(F_1 + \frac{3v^2_\perp F_2}{2v^2_{T_b} x^2} \right) \frac{\partial f_a}{\partial v_\perp} + \frac{3F_2}{2x^2} v_\perp v'_\parallel \frac{\partial f_a}{\partial v_\parallel} \right\} \right]. \qquad \text{(A.22)}
\end{aligned}$$

where $\boldsymbol{v} = \boldsymbol{v}_\parallel + \boldsymbol{v}_\perp$, $v'_\parallel = v_\parallel - U_{\parallel,b}$, $v' = \sqrt{v'^2_\parallel + v^2_\perp}$ and $x = v'/(\sqrt{2} v_{T_b})$. Here, $\bar{\nu}_{ab}$ is defined as $n_b \Gamma_{ab} / \{3(2\pi)^{3/2} v^3_{T_b}\}$ and $U_{\parallel,b}$ is the parallel fluid velocity of the species b. Note that this equation retains cross-diffusion terms as well as diagonal diffusion terms of the Dougherty operator. In addition, pulling out the mass ratio factor m_a/m_b from the dragging term explicitly reveals that standard deviation of Maxwellian at equilibrium (i.e., $T_a = T_b$) depends on mass of the incident species rather than the target species. Furthermore, the $\Gamma_{ab} m_a/m_b \propto 1/(m_a m_b)$ factor gets symmetry with respect to species. Toward the Dougherty operator, taking slow speed limit where $x \ll 1$ yields

$$\begin{aligned}
C_{ab}(f_a) &= C(f_a, f_{b,M}) \\
&= \bar{\nu}_{ab} \left[\frac{\partial}{\partial v_\parallel} \left\{ \frac{m_a}{m_b} v'_\parallel f_a + v^2_{T_b} \frac{\partial f_a}{\partial v_\parallel} \right\} + \frac{1}{v_\perp} \frac{\partial}{\partial v_\perp} v_\perp \left\{ \frac{m_a}{m_b} v_\perp f_a + v^2_{T_b} \frac{\partial f_a}{\partial v_\perp} \right\} \right], \qquad \text{(A.23)}
\end{aligned}$$

where cross diffusion terms are ordered out because $F_2(x)$ is $O\left(x^2\right)$ smaller than $F_1(x)$.

B Removal of the third order derivatives from the weighted equation

With the coefficients of the RMJ collision operator, $\mathbb{V}^{[j,k]}$ of the weighted equation, i.e., Eq. (74), contains the third order derivatives of g. To improve the numerical convergence, it is beneficial to replace the third order derivatives of g with the first order derivatives of h. With α_i for the RMJ collision operator, Eq. (74) can be written as

$$\begin{aligned}
\mathbb{V}^{[j,k]}(W) &= \Gamma \int_{\Omega^{[j,k]}} d\vec{z} \left[\frac{\partial W}{\partial v_\parallel}\frac{\partial h}{\partial v_\parallel} + \frac{1}{\mathscr{J}}\frac{\partial}{\partial v_\parallel}\left(\frac{\partial W}{\partial v_\parallel}\frac{\partial^2 g}{\partial v_\parallel^2}\mathscr{J}\right) + \frac{B_0}{B}\frac{1}{u}\frac{\partial}{\partial u}\left(\frac{\partial W}{\partial v_\parallel}\frac{\partial^2 g}{\partial v_\parallel \partial u}u\right) \right. \\
&\quad + \frac{B_0}{B}\frac{\partial W}{\partial u}\frac{\partial h}{\partial u} + \frac{B_0^2}{B^2}\frac{1}{u}\frac{\partial}{\partial u}\left(\frac{\partial W}{\partial u}\frac{\partial^2 g}{\partial u^2}u\right) + \frac{B_0}{B}\frac{1}{\mathscr{J}}\frac{\partial}{\partial v_\parallel}\left(\frac{\partial W}{\partial u}\frac{\partial^2 g}{\partial v_\parallel \partial u}\mathscr{J}\right)\Bigg] \mathscr{J} f_d^{[j,k]} \\
&= \Gamma \int_{\Omega^{[j,k]}} d\vec{z} \left[\left\{ \frac{\partial h}{\partial v_\parallel} + \frac{\partial^2 g}{\partial v_\parallel^2}\frac{1}{\mathscr{J}}\frac{\partial \mathscr{J}}{\partial v_\parallel} + \mathbb{C}_1 \right\} \frac{\partial W}{\partial v_\parallel} + \frac{\partial^2 g}{\partial v_\parallel^2}\frac{\partial^2 W}{\partial v_\parallel^2} + 2\frac{B_0}{B}\frac{\partial^2 g}{\partial v_\parallel \partial u}\frac{\partial^2 W}{\partial v_\parallel \partial u} \right. \\
&\quad \left. + \frac{B_0}{B}\left\{ \frac{\partial h}{\partial u} + \frac{\partial^2 g}{\partial v_\parallel \partial u}\frac{1}{\mathscr{J}}\frac{\partial \mathscr{J}}{\partial v_\parallel} + \mathbb{C}_2 \right\} \frac{\partial W}{\partial u} + \left(\frac{B_0}{B}\right)^2 \frac{\partial^2 g}{\partial u^2}\frac{\partial^2 W}{\partial u^2} \right] \mathscr{J} f_d^{[j,k]},
\end{aligned} \tag{B.1}$$

where

$$\begin{aligned}
\mathbb{C}_1 &\equiv \frac{B_0}{B}\frac{1}{u}\frac{\partial^2 g}{\partial v_\parallel \partial u} + \frac{B_0}{B}\frac{\partial^3 g}{\partial v_\parallel \partial^2 u} + \frac{\partial^3 g}{\partial^3 v_\parallel}, \\
\mathbb{C}_2 &\equiv \frac{B_0}{B}\frac{\partial^3 g}{\partial u^3} + \frac{\partial^3 g}{\partial v_\parallel^2 \partial u} + \frac{B_0}{B}\frac{1}{u}\frac{\partial^2 g}{\partial u^2}.
\end{aligned} \tag{B.2}$$

From Eq. (73), $\partial h/\partial v_\parallel$ and $\partial h/\partial u$ are given as

$$\begin{aligned}
\frac{\partial h}{\partial v_\parallel} &= \frac{B_0}{B}\frac{1}{u}\frac{\partial^2 g}{\partial v_\parallel \partial u} + \frac{B_0}{B}\frac{\partial^3 g}{\partial v_\parallel \partial^2 u} + \frac{\partial^3 g}{\partial^3 v_\parallel}, \\
\frac{\partial h}{\partial u} &= \frac{B_0}{B}\frac{\partial^3 g}{\partial u^3} + \frac{\partial^3 g}{\partial v_\parallel^2 \partial u} + \frac{B_0}{B}\frac{1}{u}\frac{\partial^2 g}{\partial u^2} - \frac{B_0}{B}\frac{1}{u^2}\frac{\partial g}{\partial u}.
\end{aligned} \tag{B.3}$$

With Eq. (B.3), Eq. (B.2) can be rewritten as

$$\begin{aligned}
\mathbb{C}_1 &= \frac{\partial h}{\partial v_\parallel}, \\
\mathbb{C}_2 &= \frac{\partial h}{\partial u} + \frac{B_0}{B}\frac{1}{u^2}\frac{\partial g}{\partial u}.
\end{aligned} \tag{B.4}$$

If we substitute Eq. (B.4) into Eq. (B.1), we obtain

$$\begin{aligned}
\mathbb{V}^{[j,k]}(W) &= \Gamma \int_{\Omega^{[j,k]}} d\vec{z} \left[\left\{ 2\frac{\partial h}{\partial v_\parallel} + \frac{\partial^2 g}{\partial v_\parallel^2}\frac{1}{\mathscr{J}}\frac{\partial \mathscr{J}}{\partial v_\parallel} \right\} \frac{\partial W}{\partial v_\parallel} + \frac{\partial^2 g}{\partial v_\parallel^2}\frac{\partial^2 W}{\partial v_\parallel^2} + 2\frac{B_0}{B}\frac{\partial^2 g}{\partial v_\parallel \partial u}\frac{\partial^2 W}{\partial v_\parallel \partial u} \right. \\
&\quad \left. + \frac{B_0}{B}\left\{ 2\frac{\partial h}{\partial u} + \frac{\partial^2 g}{\partial v_\parallel \partial u}\frac{1}{\mathscr{J}}\frac{\partial \mathscr{J}}{\partial v_\parallel} + \frac{B_0}{B}\frac{1}{u^2}\frac{\partial g}{\partial u} \right\} \frac{\partial W}{\partial u} + \left(\frac{B_0}{B}\right)^2 \frac{\partial^2 g}{\partial u^2}\frac{\partial^2 W}{\partial u^2} \right] \mathscr{J} f_d^{[j,k]},
\end{aligned} \tag{B.5}$$

which does not contain the third order derivatives of g, as desired.

References

[1] L. Landau, Phys. Z. Sowjetunion **10**, 154 (1936)

[2] Marshall N. Rosenbluth, William M. MacDonald and David L. Judd, Phys Rev. **107**, 1 (1957)

[3] Per Helander, Dieter J. Sigmar, Collisional Transport in Magnetized Plasmas, Cambridge University Press, 2002.

[4] P. L. Bhatnagar, E. P. Gross and M. Krook, Physical Rev. **94**, 511 (1954)

[5] A. Lenard and I. B. Bernstein, Phys. Rev. **112**, 1456 (1958)

[6] J. P. Dougherty, Phys. Fluids **7**, 1788 (1964)

[7] A. Lenard, Ann. Phys. (N.Y.) **3**, 390 (1960)

[8] R. Balescu, Phys. Fluids **3**, 52 (1960)

[9] S.P. Hirshman and D.J. Sigmar, Phys. Fluids, **19**, 1532 (1976)

[10] I. G. Abel, M. Barnes, S. C. Cowley, W. Dorland and A. A. Schekochihin, Phys. Plasmas **15**, 122509 (2008)

[11] H. Sugama, T.-H. Watanabe and M. Nunami, Phys. Plasmas **16**, 112503 (2009)

[12] H. Sugama, S. Matsuoka, S. Satake, M. Nunami and T.-H. Watanabe, Phys. Plasmas **26**, 102108 (2019)

[13] 2050 Carbon Neutrality and Green Growth Commission, www.2050cnc.go.kr

[14] International Atomic Energy Agency, www.iaea.org

[15] Jeffrey P. Freidberg, Plasma Physics and Fusion Energy, Cambridge University Press, 2007.

[16] Koichi MAKI, Journal of Nuclear Science and Technology **25** 1 (1988)

[17] J D Lawson, Proc. Phys. Soc. B **70** 6 (1957)

[18] BICKERTON, R., CONNOR, J. and TAYLOR, J. Nature Physical Science **229**, 110 (1971)

[19] M. C. Zarnstorff et al., Phys. Rev. Lett. **60**, 1306 (1988)

[20] S. Li, H. Jiang, Z. Ren, C. Xu, Abstract and Applied Analysis, **2014**, 940965 (2014)

[21] Francis F. Chen, Introduction to Plasma Physics and Controlled Fusion, Springer, 2016.

[22] Jan S. Hesthaven and Tim Warburton, Nodal Discontinuous Galerkin Methods, Springer, 2008.

[23] Cockburn, B., Z. angew. Math. Mech., **83**, 731-754 (2003)

[24] Eric Leon Shi, "Gyrokinetic Continuum Simulation of Turbulence in Open-Field-Line Plasmas" (Ph.D. diss., Princeton University, 2017)

[25] L. Chacón,, D. C. Barnes, D. A. Knoll and G. H. Miley, J. Comput. Phys **157**, 618 (2000)

[26] L. Chacón,, D. C. Barnes, D. A. Knoll and G. H. Miley, J. Comput. Phys **157**, 654 (2000)

[27] W. T. Taitano, L. Chacón, A. N. Simakov and K. Molvig, J. Comput. Phys. **297**, 357 (2015)

[28] Andras Pataki and Leslie Greengard, J. Comput. Phys. **230**, 7840 (2011)

[29] E. S. Yoon and C. S. Chang, Phys. Plasmas **21**, 032503 (2014)

[30] R. Hager, E. S. Yoon, S. Ku, E. F. D'Azevedo, P. H. Worley and C. S. Chang, J. Comput. Phys. **315**, 644 (2016)

[31] E. Hirvijoki and M. F. Adams, Phys. Plasmas **24**, 032121 (2017)

[32] M. Francisquez, T. N. Bernard, N. R. Mandell, G. W. Hammett and A. Hakim, Nucl. Fusion **60**, 096021 (2020)

[33] Ammar Hakim, Manaure Francisquez, James Juno and Gregory W. Hammett, J. Plasma Phys. **86**, 905860403 (2020)

[34] Takashi Shiroto, Akinobu Matsuyama, Nobuyuki Aiba and Masatoshi Yagi, J. Comput. Phys. **449**, 110813 (2022)

[35] Gahyung Jo, Jae-Min Kwon, Janghoon Seo and Eisung Yoon, Comput. Phys. Comm. **273**, 108265 (2022)

[36] N.R. Mandell, A. Hakim, G.W. Hammett, and M. Francisquez, J. Plasma Phys. **86**, 38 (2020)

[37] E. A. Belli and J. Candy, Plasma Phys. Control. Fusion **59**, 045005 (2017)

[38] T.S. Hahm, Physics of Fluids **31**, 2670 (1988)

[39] Q. Pan and D.R. Ernst, Phys. Rev. E **99**, 023201 (2019)

[40] E.L. Shi, G.W. Hammett, T. Stoltzfus-Dueck, and A. Hakim, J. Plasma Phys. **83**, 905830304 (2017)

[41] B. Cockburn, S. Hou, C.-W. Shu, The Runge-Kutta Local Projection Discontinuous Galerkin Finite Element Method for Conservation Laws. IV: The Multidimensional Case, Mathematics of Computation **54**, 545 (1990)

[42] W. X. Wang, N. Nakajima, M. Okamoto and S. Murakami, Plasma Phys. Control. Fusion **41**, 1091 (1999)

[43] Y. Idomura, H. Urano, N. Aiba, and S. Tokuda, Nucl. Fusion **49**, 065029 (2009)

[44] S. Satake, Y. Idomura, H. Sugama and T. H. Watanabe, Comput. Phys. Comm. **181**, 1069 (2010)

[45] W.T. Taitano, L. Chacón, and A.N. Simakov, J. Comput. Phys. **339**, 453 (2017)

[46] D. Daniel, W.T. Taitano, and L. Chacón, Comput. Phys. Comm. **254**, 107361 (2020)

[47] A. S. Richardson, NRL Plasma Formulary, National Research Laboratory, 2019.

[48] C. S. Chang and F. L. Hinton, Phys. Fluids **25**, 1493 (1982)

[49] Matt Landreman and Darin R Ernst, Plasma Phys. Control. Fusion **54**, 115006 (2012)

[50] P Donnel, C Gheller, S Brunner, L Villard, E Lanti, N Ohana1 and M Murugappan, Plasma Phys. Control. Fusion **63**, 025006 (2021)

[51] O. Sauter, C. Angioni and Y. R. Lin-Liu , Phys. Plasmas **6**, 2834 (1999)

[52] F. L. Hinton and M. N. Rosenbluth Plasma Phys. Control. Fusion **41**, A653 (1999)

[53] Y. Xiao, P. J. Catto and K. Molvig, Phys. Plasmas **14**, 032302 (2007)

[54] G.D. Conway, A.I. Smolyakov, and T. Ido, Nucl. Fusion **62**, 013001 (2022)

[55] Y. Li and Z. Gao, Nucl. Fusion **55**, 043001 (2015)

[56] Z. Gao, K. Itoh, H. Sanuki, and J.Q. Dong, Physics of Plasmas **15**, 072511 (2008)

[57] H. Sugama and T.-H. Watanabe, Physics of Plasmas 13, 012501 (2006)

[58] S. Satake, H. Sugama, and T.-H. Watanabe, Nucl. Fusion 47, 1258 (2007)

[59] X.Q. Xu, E. Belli, K. Bodi, J. Candy, C.S. Chang, R.H. Cohen, P. Colella, A.M. Dimits, M.R. Dorr, Z. Gao, J.A. Hittinger, S. Ko, S. Krasheninnikov, G.R. McKee, W.M. Nevins, T.D. Rognlien, P.B. Snyder, J. Suh, and M.V. Umansky, Nucl. Fusion 49, 065023 (2009)

[60] W.T. Taitano, L. Chacón, and A.N. Simakov, J. Comput. Phys. **318**, 391 (2016)

[61] Richard D. Hazeltine and Francois L. Waelbroeck, The Framework of Plasma Physics, Perseus books, 1998.

Acknowledgements

"Be who you needed when you were younger". 제가 좋아하는 말 중 하나입니다. 학위 과정을 지나오면서 얼마나 가까워졌는지는 모르겠지만, 조금이라도 제가 필요로 했던 사람에 다가갔다고 생각합니다. 그러기까지 여러 사람의 도움이 있었습니다.

가장 먼저 경애하는 지도교수, 윤의성 교수님께 감사 인사를 드리고 싶습니다. 교수님 덕분에 학부 인턴 시절부터 학위를 마치기까지 정말 많은 성장을 했습니다. 단순히 전공 분야뿐만 아니라 인생과 진로에 대해서도 함께 얘기할 수 있어서 몹시 유익하고 즐거웠습니다.

다음으로 학위 심사를 맡아주신 김희령 교수님과 허민섭 교수님께도 감사합니다. 교수님들의 질문과 의견이 제 식견을 키우는 데 큰 도움이 되었습니다.

그리고 학위논문을 작성하는 데 정말 큰 도움을 주신 서장훈 박사님께도 감사 인사를 드립니다. 박사님과의 협업이 끝나 아쉬울 따름입니다.

또한 남아 있는 연구실 구성원들에게 고마움과 응원의 말을 보냅니다. 문태욱 형님과 염성필 형님 덕분에 연구실 생활이 건설적이었으며, 박사까지의 여정이 순탄하기를 바랍니다.

거듭하여 학부 시절부터 즐거움을 나눠준 정훈이와 상훈이에게도 마찬가지로 고마움과 응원의 마음을 남깁니다.

마지막으로 무한한 애정을 보내주신 어머니께 사랑한다는 말을 전합니다. 어머니의 지지가 없었다면 이렇게 성공적인 마무리를 하지는 못했을 것입니다.